



**Three-Dimensional Turbulence Measurements
in the Atmospheric Surface Layer:
Experimental Design and Initial Analysis**

**by David Tofsted, Sean O'Brien, Cheryl Klipp,
Jimmy Yarbrough, David Quintis, Robert Brice,
Manuel Bustillos, Scott Elliott, and Edward Creegan**

ARL-TR-4953

September 2009

NOTICES

Disclaimers

The findings in this report are not to be construed as an official Department of the Army position unless so designated by other authorized documents.

Citation of manufacturer's or trade names does not constitute an official endorsement or approval of the use thereof.

Destroy this report when it is no longer needed. Do not return it to the originator.

Army Research Laboratory

White Sands Missile Range, NM 88002-5513

ARL-TR-4953

September 2009

Three-Dimensional Turbulence Measurements in the Atmospheric Surface Layer: Experimental Design and Initial Analysis

**David Tofsted, Sean O'Brien, Cheryl Klipp,
Jimmy Yarbrough, David Quintis, Robert Brice,
Manuel Bustillos, Scott Elliott, and Edward Creegan
Computational Information Sciences Directorate, ARL**

REPORT DOCUMENTATION PAGE			<i>Form Approved</i> OMB No. 0704-0188		
Public reporting burden for this collection of information is estimated to average 1 hour per response, including the time for reviewing instructions, searching existing data sources, gathering and maintaining the data needed, and completing and reviewing the collection information. Send comments regarding this burden estimate or any other aspect of this collection of information, including suggestions for reducing the burden, to Department of Defense, Washington Headquarters Services, Directorate for Information Operations and Reports (0704-0188), 1215 Jefferson Davis Highway, Suite 1204, Arlington, VA 22202-4302. Respondents should be aware that notwithstanding any other provision of law, no person shall be subject to any penalty for failing to comply with a collection of information if it does not display a currently valid OMB control number. PLEASE DO NOT RETURN YOUR FORM TO THE ABOVE ADDRESS.					
1. REPORT DATE (DD-MM-YYYY) September 2009		2. REPORT TYPE Final		3. DATES COVERED (From - To) April-June 2008	
4. TITLE AND SUBTITLE Three-Dimensional Turbulence Measurements in the Atmospheric Surface Layer: Experimental Design and Initial Analysis			5a. CONTRACT NUMBER		
			5b. GRANT NUMBER		
			5c. PROGRAM ELEMENT NUMBER		
6. AUTHOR(S) David Tofsted, Sean O'Brien, Cheryl Klipp, Jimmy Yarbrough, David Quintis, Robert Brice, Manuel Bustillos, Scott Elliott, and Edward Creegan			5d. PROJECT NUMBER CB1694		
			5e. TASK NUMBER		
			5f. WORK UNIT NUMBER		
7. PERFORMING ORGANIZATION NAME(S) AND ADDRESS(ES) U.S. Army Research Laboratory Computational and Information Sciences Directorate Battlefield Environment Division (ATTN: RDRL-CIE-D) White Sands Missile Range, NM 88002-5501			8. PERFORMING ORGANIZATION REPORT NUMBER ARL-TR-4953		
9. SPONSORING/MONITORING AGENCY NAME(S) AND ADDRESS(ES) U.S. Army Research Laboratory 2800 Powder Mill Road Adelphi, MD 20783-1145			10. SPONSOR/MONITOR'S ACRONYM(S)		
			11. SPONSOR/MONITOR'S REPORT NUMBER(S)		
12. DISTRIBUTION/AVAILABILITY STATEMENT Approved for public release; distribution is unlimited.					
13. SUPPLEMENTARY NOTES					
14. ABSTRACT The Three-Dimensional Turbulence Structure (3DTS) Test conducted in the spring of 2008 consisted of a series of measurements designed to sense three-dimensional temperature and wind turbulence structures in the near surface atmosphere. The means of performing this characterization task involved time dependent measurements taken using an array of 23 RM Young 81000 sonic anemometers. Data were sampled at 20 Hz at positions across a two-dimensional grid mounted on three towers oriented perpendicular to the expected prevailing wind. Observations were made over a 60-day period with a number of multiday sequences of continuous observations between April and June 2008. The experiment was conducted at White Sands Missile Range, NM, under dry conditions with periodic strong wind events. The dry conditions were conducive to high variations in turbulent stability conditions over diurnal cycles. Cloud coverage was minimal throughout the period. This report documents the major features of the test, including the setup, tower configuration, wind, temperature, and stability states observed, and data availability. In all, over 300 hours of complete sensor data sets were available. Stability conditions present, as characterized by the 2 m temperature gradient, ranged between -0.35 C/m during the daytime to upwards of +0.75 C/m at night, indicating significant periods of strong stable conditions.					
15. SUBJECT TERMS turbulence, stability, surface layer, characterization					
16. SECURITY CLASSIFICATION OF:			17. LIMITATION OF ABSTRACT	18. NUMBER OF PAGES	19a. NAME OF RESPONSIBLE PERSON David Tofsted
a. REPORT Unclassified	b. ABSTRACT Unclassified	c. THIS PAGE Unclassified			UU

Contents

List of Figures	iv
List of Tables	v
Preface	vi
Acknowledgments	vii
Executive Summary	ix
1. Introduction	1
2. Array Design and Data Acquisition	5
2.1 Site Description.....	8
2.2 Data Acquisition and Handling.....	12
3. Data Inventory	13
3.1 Data availability	13
3.2 Wind speed statistics.....	14
3.3 Application of wind azimuth and speed filtration.....	16
3.4 Stability and ambient temperature considerations	18
4. Analysis of Stability and Anisotropy Conditions Observed	21
4.1 Stability metrics	21
4.2 Anisotropy metrics.....	24
4.3 Correlation of anisotropy with stability and other parameters.....	26
5. Conclusions	30
6. References	32
Appendix. Tower Construction Images	35
List of Symbols, Abbreviations, and Acronyms	41
Distribution	42

List of Figures

Figure 1. Tower spacing and sonic anemometer sensor placement geometry.....	3
Figure 2. Building 19472 compound on WSMR, NM, its near environs, and the approximate location and orientation of the two-dimensional array 167 ft. away relative to the compound fenceline.	4
Figure 3. View of the 4 m–12 m tower array levels looking southeast.	6
Figure 4. View of complete tower array looking west into direction of prevailing winds.	6
Figure 5. View of lowest tower array level, Li-Cor hygrometer electronics boxes and 2 m and 4 m “fetch” array levels on right (south) of tower array.	7
Figure 6. View looking up the “fetch” portion of the array.....	8
Figure 7. Terrain tilt calculations evaluated using two different methods.	10
Figure 8. Graphical comparison between surveyed sonic anemometer locations and orthogonal 2 m position separations.	12
Figure 9. Graphical history of data availability during the measurement period.	14
Figure 10. Graphical history of hourly mean wind speed (blue) observed during the test.....	15
Figure 11. Scatter plot of streamwise versus crosswind standard deviations of wind speed about the mean wind vector.	16
Figure 12. Scatter plots a, b, and c of X and Y hourly averaged mean wind components during each month of the test period (April to left and June to right).	17
Figure 13. Filtered hourly data sets selecting out hours according to increasingly discriminating criteria.....	17
Figure 14. Mean hourly wind speeds plotted relative to time of day to show available wind versus time states available.	18
Figure 15. Mean hourly temperature values sensed by the 4m flux profile sensor during the experimental measurement period (orange equals April, red equals May, brick red equals June). 20	
Figure 16. Least squares computed mean vertical temperature gradients (C/m) at 2 m height for April. Blue line: 1-minute average results. Green line: ½-hour averaged 1-minute results.....	22
Figure 17. Least squares computed mean vertical temperature gradients (C/m) at 2 m height for May. Blue line: 1-minute average results. Green line: ½-hour averaged 1-minute results.....	22
Figure 18. Least squares computed mean vertical temperature gradients (C/m) at 2 m height for June. Blue line: 1-minute average results. Green line: ½-hour averaged 1-minute results.....	23

Figure 19. Scatter plot of measured hourly mean horizontal winds at 4 m and estimated mean vertical temperature gradients at a 2 m height calculated from least-squares analysis (A/2 from the least squares analysis).....	23
Figure 20. Isotropy parameter F as a function of length scale for day (left) and night (right) cases based on data collected at the 10 m level.	26
Figure 21. Diurnal dependence of L_F length scale for 10 Jun 07 intercomparison data.....	27
Figure 22: Scatter graph of the first and second largest TKE eigenvalues.....	28
Figure 23. Probability distribution of the angle created between the mean wind direction and the principal eigenvector of the TKE ellipsoid.	29
Figure 24. Distribution plot of the angle between the projection of the third eigenvector onto the mean wind axis and then determining the angle between this projection and the vertical axis.	30
Figure A-1. Scott Elliott holds sonic with its data/power pigtail, with Sean O'Brien and Edward Creegan by 40 ft tower.	35
Figure A-2. David Tofsted, Robert Brice, and Scott Elliot inspect mounting bracket on tower boom.....	35
Figure A-3. Cross bracing system shown on mounted tower.	36
Figure A-4. Detailed view of mounting method for sonic anemometer, hygrometer and thermistor on flux profile boom.	36
Figure A-5. Fully wired and instrumented flux profile tower awaits setup.....	37
Figure A-6. Sean O'Brien adjusts spacing of Li-Cor fast hygrometer with sonic anemometer to permit latent heat flux measurements.....	37
Figure A-7. Jimmy Yarbrough in foreground adjusting turnbuckle while performing final adjustments on flux profile tower for leveling.	38
Figure A-8. David Quintis stands between towers and Robert Brice wires instruments inside data acquisition box.....	38
Figure A-9. Robert Brice and Edward Creegan inspect completed array looking west toward Baylor Pass (far left), Baylor Peak (just under [0, 4] flux profile sensors), San Augustin pass (behind central mast), and San Augustin Peak (just under [10, 04] sonic anemometer). .	39

List of Tables

Table 1. Triangulated coordinates of array sensors rotated into a plane of minimal Y-Coordinate variation.....	11
--	----

Preface

Over the past several years U.S. Army Research Laboratory (ARL) personnel have collected data series used to generate various turbulent one-dimensional (1D) time and spatial spectra during mission-related field tests. These spectra exhibited unexpected behaviors at low frequency. Typically it is assumed that turbulence is isotropic (directionally independent) and homogeneous (positionally independent). Theory then indicates these turbulent spectra feature an inertial subrange behavior at moderate frequencies, exhibiting a characteristic $-5/3$ power law dependence. At low frequencies this power law dependence should transition to a frequency independent flat spectral behavior associated with the “energy containing region.” Spectral behavior in the low frequency domain is very important because it has the potential to affect the performance of Army electro-optical imaging systems, as well as modifying the simulated coupling of surface based fluxes to mesoscale models of the atmosphere.

The key gap in such models is the assumption of isotropy. For near-surface conditions, this assumption is inaccurate. For example, non-zero net fluxes between the atmosphere and the surface require anisotropy. To improve spectral models, the experiment described herein was proposed to provide a data base of anisotropic measurements sufficient to improve our knowledge and modeling capabilities of the near-surface environment under varying atmospheric stability and wind conditions.

Data analysis from this field test should be suitable for evaluating the three-dimensional (3D) structure of anisotropic turbulent structures up to the size scales measured during the test. In particular, Taylor’s frozen turbulence hypothesis can be used to extrapolate temporal fluctuation series sensed over an array of 3D sonic anemometers into a third dimension of measurement that, when coupled to the two dimensional (2D) extent of the tower system itself, characterizes turbulent structures over a spatial volume. The data analysis described herein is the initial examination for this valuable data set. Comparable studies performed by independent investigators in disparate geographic localities may also be examined with this data set. Future analysis efforts based on this data may then focus on anisotropies in spatial turbulence fields as functions of time of day and stability.

Aside from the 3D analysis outlined in this report, the archived body of data from this test will be a useful resource for additional analysis of 1D and 2D time series, spatial series, and vertical profiles of water vapor fluctuations. This data set covers a drier season than water vapor fluctuation data collected during prior field tests at White Sands Missile Range (WSMR), NM.

Acknowledgments

This work was supported by the Defense Threat Reduction Agency under project number CB1694, the Turbulence in the Stable Boundary Layer program.

INTENTIONALLY LEFT BLANK.

Executive Summary

The Three-Dimensional Turbulence Structure (3DTS) Test was performed at White Sands Missile Range (WSMR), NM, in the late spring of 2008. There were several objectives of this experiment: to investigate the degree of anisotropy and of horizontal inhomogeneity of atmospheric turbulence near the ground; to determine whether these anomalies can explain or predict the disparities observed between theories of Fourier spectra of atmospheric turbulence and measured turbulence spectra; and to investigate the effects anisotropy and horizontal inhomogeneity might have on atmospheric dispersion.

The genesis of this investigation arose over several years of analysis of Fourier spectra of time series of atmospheric turbulence data collected during a series of field tests. Classical models of atmospheric turbulence invoke the assumptions of isotropic and homogeneous conditions. Yet spectra generated using time series failed to exhibit low frequency behavior that matched the classical models. Explanations of this failure led to the question of how anisotropic and inhomogeneous conditions might be detected. Here the prior efforts of research groups at the National Center for Atmospheric Research (NCAR) became salient in our planning.

NCAR in collaboration with several university researchers conducted a series of experiments involving arrays of sonic anemometers, the first of which was termed the Horizontal Array Turbulence Study (HATS). The HATS field program¹ was designed to study the correlations between spatially-filtered and subfilter-scale (SFS) turbulence.² HATS used a transverse array technique proposed by Tong et al., 1998,³ for two-dimensional, horizontal filtering of turbulence variables. The HATS measurement configuration consisted primarily of a horizontal line of nine equally-spaced sonic anemometers mounted at one height and a parallel line of five sonic anemometers at a second height. The primary driver for these studies was the improvement of Large Eddy Simulation (LES) models.

In our case, the primary objective was the understanding of three-dimensional (3D) anisotropic turbulence structure in the atmospheric surface layer. Though the two studies are similar, the overall spacing of the HATS sensors tended to concentrate measurements at the subgrid-scale. Conversely, our effort sought to understand the transition in structure that occurs between the inertial subrange scale, which presumably extends to approximately the distance associated with isotropic turbulence (less than or equal to the height of the observation point above the surface)

¹ Horst, T. W.; Kleissl, J.; Lenschow, D. H.; Meneveau, C.; Moeng, C.-H.; Parlange, M. B.; Sullivan, P. P.; Weil, J. C. HATS: Field Observations to Obtain Spatially Filtered Turbulence Fields from Crosswind Arrays of Sonic Anemometers in the Atmospheric Surface Layer. *J. Atmos. Sci.* **2004**, 61, 1566–1581.

² Sullivan, P. P.; Horst, T. W.; Lenschow, D. H.; Moeng, C.-H.; Weil, J. C. Structure of subfilter-scale fluxes in the atmospheric surface layer with application to large-eddy simulation modeling. *J. Fluid Mech.* **2003**, 482, 101–139.

³ Tong, C.; Wyngaard, J.C., Khanna, S.; Brasseur, J.G. Resolvable-and subgrid-scale measurement in the atmospheric surface layer: Technique and issues. *J. Atmos. Sci.* **1998**, 55, 3114–3126.

and the decorrelations that occur at size scales extending into the energy-containing range. Hence, our minimum sensor height is 2 m, and our maximum sensor separation is 14 m, a length scale long enough that transversely separated measurements should show significant decorrelations within the space of the grid.

The importance of this investigation is in its application to system performance models which rely on the aforementioned isotropic homogeneous spectral modeling approach. While it is not yet clear what the ultimate impact of the modification of such spectra will have on sensor performance predictions, it is clear that today's models are incorrectly reporting the effects of the atmosphere.

The 3DTS experiment entailed the construction of a two-dimensional grid of sonic anemometer wind sensors oriented transversely to the mean wind. The three components of the wind vector and temperature were sampled 20 times per second over a two-month period. Three-dimensional (3D) effects can be inferred based on Taylor's frozen turbulence hypothesis. Taylor's frozen turbulence hypothesis states that fluctuations in advecting turbulence fields as detected by a fixed observer can be considered relatively stationary in the field because the eddies are fixed or frozen into the mean flow. Therefore they do not change considerably as they are advected. This hypothesis allows the time series recorded at a fixed point to be interpreted as spatial fluctuations along a line in the mean flow direction. This hypothesis assumes the mean wind carries turbulent wind, temperature, and humidity fluctuations through the wind sensor positions. Temporal records of fluctuations can thus be used to generate fully 3D representations of the atmospheric fluctuation patterns.

WSMR is located in the heart of the Chihuahuan desert. Diurnal temperature variations can reach forty degrees Fahrenheit. Over 300 hours of data were found to be suitable for further study. These featured a wide range of surface stability conditions that allowed analysis of a range of lapse and inversion conditions that could be correlated to turbulence anisotropy metrics. As a result a robust data set was produced that will provide a basis for future analysis work in study of the anisotropy and inhomogeneity issues outlined above.

From an Army perspective, daytime conditions can lead to rapid dissipation of atmospheric contaminants (dust, smoke, etc.). Nighttime stable conditions can trap contaminants within the surface inversion layer and concentrate materials at long distances from their sources. Thus there are clearly operational conditions under which the characterization of such flows is significant, and the work of analysis of these data sets will prove valuable in understanding the nature of small-scale variations and anisotropic effects under tactically significant conditions.

1. Introduction

For many years the U.S. Army Research Laboratory's (ARL) Battlefield Environment Division (BED) has worked in the area of near-earth atmospheric characterization of turbulence.

Turbulence impacts many aspects of Army operations, but particularly affects the transport and diffusion of chemical and smoke munitions, battlefield dust, and the operational quality of ground-to-ground electro-optical systems and lasers. The ARL BED has had a long standing, strong working relationship with the U.S. Army Space and Missile Defense Command's High Energy Laser System Test Facility (HELSTF) located on White Sands Missile Range (WSMR), NM. One such collaboration between BED and HELSTF was during the NATO Research Technology Group 40 (RTG-40) active imaging land field trials experiment performed at the HELSTF range on WSMR, NM, in November of 2005 (Tofsted et al., 2006). The objective of that test was to intercompare the capabilities of several active range-gated laser imaging systems under varying turbulence conditions. ARL and HELSTF provided extensive meteorological and scintillometer instrumentation support during that test.

One hardware component of the meteorological characterization effort for the RTG-40 test was a 9 m meteorological (met) tower located near the center of the 2 km propagation range. Four RM Young 81000 sonic anemometer sensors were arranged at 2 m vertical intervals on the tower. Data were collected at a sampling rate of 20 Hz. Data from each sensor were used to generate temperature spectra using Taylor's frozen turbulence hypothesis. According to this approximation, turbulent eddies are considered to be embedded within a mean translating wind field with zero internal relative motion (e.g., Hill, 1996). Temporal measurements can therefore be interpreted as a spatially varying series.

We expected that the spatial spectra developed from the RTG-40 sonic anemometer instruments under the Taylor hypothesis would conform to the accepted theory of turbulent fluctuations. According to this theory, as articulated by Kaimal et al., 1972, spectral scales should divide into three categories: the dissipation subrange, the inertial subrange, and the energy containing range. The length scales approximately dividing these three ranges are termed the inner scale (on the order of a few millimeters) and the outer scale (approximately the height of the measurement point above the local terrain). For length scales associated with the inertial subrange (on the order of a few meters or less) the turbulent spectra should exhibit a characteristic $-5/3$ power law dependence associated with the Kolmogorov (1941) theory. For larger size scales, the one-dimensional spectral behavior should reach a plateau at low frequencies (e.g., Tofsted, 2000). However, a number of the spectral examples computed from the RTG-40 test did not reflect the expected leveling-off behavior. Instead of leveling off, the spectra continued to increase as frequency decreased, sometimes at approximately the same $-5/3$ dependence as for the inertial

range. The equivalent wavelengths of these frequencies would be hundreds of meters long, a consequence thoroughly at odds with the isotropic assumption of Kolmogorov's theory.

A working hypothesis to explain this behavior is that the fluctuations measured by our sensors consisted of a combination of high frequency (small scale) third-dimensional (3D) isotropic fluctuations and low frequency (longer scale) two-dimensional (2D) anisotropic fluctuations. However, knowing that such mixed states exist is one issue, predicting the strength, cutoff scales, and energy cascade mechanisms between the 2D and 3D turbulence is another. The vertical sensor array data from RTG-40 clearly point to the potential for anisotropy between the vertical direction and the two horizontal directions. However, there may also be anisotropy between fluctuations that occur along the mean wind axis and in the crosswind direction. Unfortunately, winds measured at different heights on a single tower cannot be used to discriminate horizontally varying effects from vertically varying ones. Hence, a means of collecting measurements in 3D is needed. Data from a single instrumented tower, when combined with Taylor's hypothesis, provides both vertical and horizontal structure for a vertical slice of atmosphere along the wind run. Thus to measure 3D effects one need only set up a 2D array of wind sensors located on towers placed along the crosswind direction. Such an array would also support the study of horizontal inhomogeneities present in the wind field at the scale of the experimental grid.

For the best use of measurement space, the 2D array was oriented such that it was perpendicular to the prevailing wind direction. In addition to the main sonic anemometer array, the initial experiment design included a separate upwind "fetch" array that would characterize the conditions prior to the wind field reaching the 2D array. However, previous similar studies (for example, the Horizontal Array Turbulence Study [HATS], sponsored by the National Center for Atmospheric Research [NCAR]) found that the information from the fetch array was consistent with information from the main array (Horst et al., 2004; Sullivan et al., 2003). HATS and its follow-on studies were designed to study the correlations between spatially-filtered and subfilter-scale (SFS) turbulence. Based on these studies it was deemed more practical to incorporate this fetch array functionality into the main array itself.

However, the HATS experiments focused on subgrid scales, whereas our interest was in the transition from the inertial subrange to the energy containing range. Hence, while HATS concentrated on sensor separations of 0.5 m and a maximum separation on the order of 4.0 m, we selected a minimum horizontal sensor separation of 2 m that was on the order of the center of the inertial range and extend the measurement range outward to distances of 14 m, beyond the outer scale.

From an Army perspective, it should also be recognized that the largest scale motions contribute the most energy to turbulent transport and dispersion. At these scales, for near-surface applications, the theoretical assumptions of isotropy and horizontal homogeneity clearly do not hold well. Therefore, anisotropy and horizontal inhomogeneity effects are both likely to make large contributions to the nature and degree of transport and dispersion near the ground.

During the planning stages for this test, analyses were performed to characterize the degree of anisotropy present at different scales. The transition in turbulence properties between 3D isotropic and 2D anisotropic flow was studied using a metric originally developed by Lumley (1978). The evaluation of this parameter could then be performed at different averaging intervals using a multiscale analysis technique described by Howell and Mahrt (1997). The results of these analyses are discussed in detail in section 4.

Here we merely summarize the results of those analyses: A clear transition in the degree of anisotropy in the wind data was found to occur between approximately the height of the measurement point above the ground and a length approximately three times this height (between 10 m and 30 m for the data analyzed from sensors at 10 m above ground level [AGL], as shown in figure 20). Below this transition scale the turbulent fluctuations exhibited isotropic character. Above this scale the turbulence increasingly exhibited a 2D nature. To study the fully 3D properties of the near-surface atmosphere a new test was proposed: the Three-Dimensional Turbulence Structure (3DTS) Test.

The geometry of the 2D anemometer array to support such a test is shown in figure 1. Initially, an array of six meteorological towers spaced at 2–4 m intervals was envisioned.

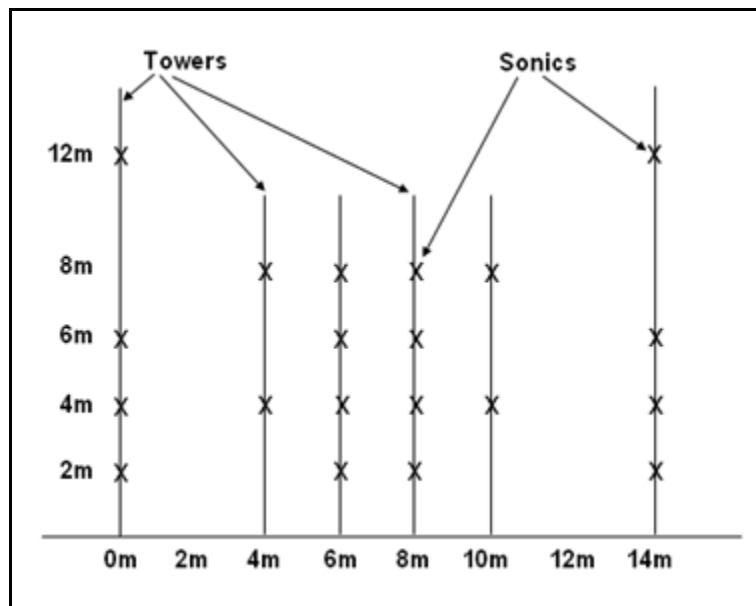


Figure 1. Tower spacing and sonic anemometer sensor placement geometry.

The objective of this sensor placement geometry was to obtain a diverse series of sensor separation distances in different directions with a minimum of sensors, while providing redundant sensor spacings and levels.

To specify sensor positions, a coordinate system was established such that the lower-leftmost sensor was defined to be at coordinate $(x, y, z) = (0 \text{ m}, 0 \text{ m}, 2 \text{ m})$ in a system in which the x axis

represented an in-array horizontal component running at approximately 26° relative to True North. The y component was a cross-array horizontal axis oriented into the direction of the prevailing wind (at running approximately 296° True). The z component measured approximately vertically upward from the surface. Thus, if we were considering correlations between sensor measurements of wind and/or temperature fluctuations at level $z = 2$ m with those at $z = 4$ m for a horizontal separation of 2 m, the grid of figure 1 would provide the possibilities of sensor $(x, z) = (4, 4)$ paired with $(6, 2)$, $(6, 2)$ paired with $(8, 4)$, $(6, 4)$ paired with $(8, 2)$, and $(8, 2)$ paired with $(10, 4)$. Given horizontally homogenous conditions, these four sensor pairs should exhibit similar correlation properties. When horizontal inhomogeneities are present these results will differ. Similarly, multiple copies of vertical and horizontal separations of 2 m, 4 m, 6 m, 8 m, and 10 m are also present. The wide duplication of selected distances between horizontally and vertically separated sensor pairs provides both statistical comparison possibilities and a data quality check.

For the test location, the WSMR range was believed to feature numerous possible sites, but a site near the ARL BED building 19472 compound was chosen for convenience, utility, and suitability. An overhead view of the region near the 19472 building compound is shown in figure 2. The array system was situated ~ 167 ft WNW of the compound fenceline.



Figure 2. Building 19472 compound on WSMR, NM, its near environs, and the approximate location and orientation of the two-dimensional array 167 ft. away relative to the compound fenceline.

The dark dots scattered about the site are mesquite bushes approximately 2 m high. A thicket of these bushes is contained within a shallow arroyo to the west and south of the site. For perspective, Bldg. 19472 measures 44 ft × 32 ft (the building's shadow is visible within the compound), the southeast fenceline measures 201 ft, and the NNE fenceline measures 136 ft.

The experiment took place during the late spring of 2008. This time of the year was selected because in general dry weather conditions prevail throughout the period from March through June in southern New Mexico. This season can also feature periods of high wind events. Cloud cover is usually also minimal during this period. Because of these dry conditions, the main heat fluxes at the surface are more easily characterized than would be possible during periods when rainfall could alter the Bowen ratio. Thus, although fast hygrometer sensors were used to sense the humidity variations, the latent heat fluxes were considered a minimal contributor to the overall heat budget.

Further details of the experimental design and setup are contained in section 2. A general overview of the meteorological conditions encountered during the test is discussed in section 3. Section 4 then includes an initial analysis of stability variability during the test and general analysis of the mean aspects of anisotropy of wind conditions measured.

2. Array Design and Data Acquisition

Following the planning and initial analyses of 2007, preparation work for assembling the tower array began in early 2008. One of the first major changes from the original design involved the tower arrangement. Initially it was anticipated that six profile towers would be necessary, using the HATS measurement configuration as a guide. However, it was recognized that the same measurements could be performed using long horizontal booms connected to only three towers: two 40-ft towers at each end, and a 30-ft tower in the center. There was also a major concern that due to the high wind conditions frequently seen during the spring, there was a possibility that the high resolution wind data could be contaminated by tower vibration effects. To reduce this possibility, a tensioned bracing system was used to stabilize each lateral tower boom. This approach involved attaching two tensioned wires from the middle of each boom to the structural tubing of the tower above and below the boom (see close-ups in figures A-3 and A-4 in appendix A). The general setup of the towers is shown in figures 3–5.



Figure 3. View of the 4 m–12 m tower array levels looking southeast.

Based on the strategy outlined in the previous section, the southern-most vertical column of sensors was chosen to also represent the “fetch” tower. In addition to the sonic anemometers, shielded thermistors were placed at heights 2, 4, 8, and 12 meters, and Li-Cor fast hygrometers were placed at 2, 4, and 8 meters along this column. An extra sonic anemometer was also placed at 8 meters so that the latent heat flux could be evaluated at all three Li-Cor levels. Extra sonic sensors were also added at the (4, 2) and (10, 2) locations to better populate the $6\text{ m} \times 6\text{ m}$ center.

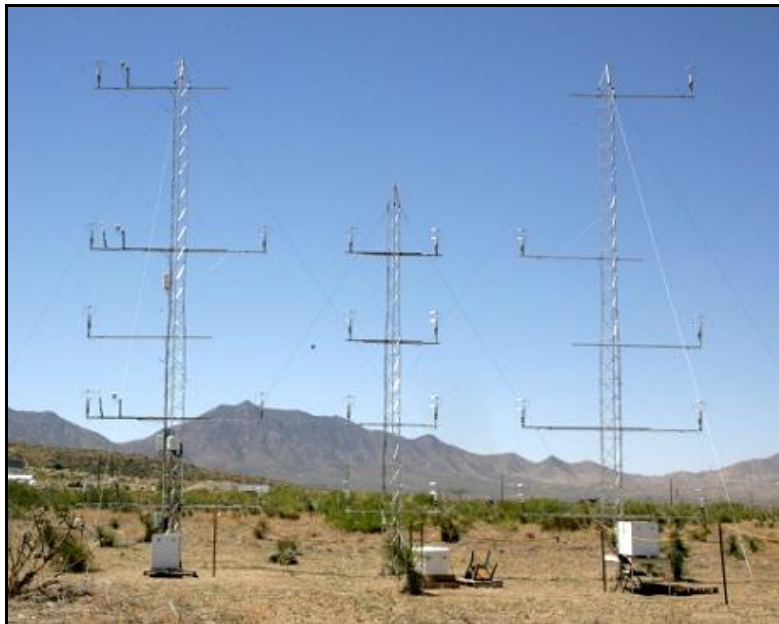


Figure 4. View of complete tower array looking west into direction of prevailing winds.



Figure 5. View of lowest tower array level, Li-Cor hygrometer electronics boxes and 2 m and 4 m “fetch” array levels on right (south) of tower array.

Note: Visible are sonic anemometers, Li-Cor hygrometer sensor heads, and shielded thermistor sensors.

Adjacent to the southern end of the array, a Kipp-and-Zonen CNR-1 four-component radiometer was placed. In addition, 1 meter and 6 inch level thermistors were set up just to the south of the “fetch” line to permit extension of the temperature profile down to a level comparable to the roughness height. These two sensors can be seen at the far left side of figure A-9 of the appendix. Figure 6 shows a view looking up the “fetch” tower. Here we note that the prevailing incident wind is from the left in the picture. Thus, the open sides of the anemometers are oriented into the mean wind direction, reducing any wake effects due to the sensor heads.



Figure 6. View looking up the “fetch” portion of the array.

2.1 Site Description

The region surrounding the building 19472 compound is relatively flat and featureless terrain characteristic of the Chihuahuan desert. The dirt is alluvial, derived from sand eroded from the nearby Organ Mountains. Due to the proximity of the mountains there is a slight terrain tilt that affects the effective local vertical for wind flow calculations.

Although the site is nearly flat, there are a few perturbing features to optimal smooth-terrain wind flow. These are located primarily to the east-southeast and the southwest of the location of the array. The 19472 compound, as shown in figure 1, consists of the single story main building surrounded by a number of parked trailers, small storage shelters, vehicles, a Morgan building, and a chain-link fence enclosure. The southwest corner of building 19472 is 73 ft from the WNW corner of the fence line. From this point in the fenceline to the array line was then 167 ft, for a total distance from the building to the array line of approximately 73 m. Using a nominal building height of 4 m, the height-to-distance (aspect) ratio is 0.055. Using a nominal threshold of this ratio as 0.1 to avoid obstruction effects, the building and its environs would thus not be expected to produce a significant effect on the sensed winds. Even so, in the subsequent analysis we filter out any winds arriving at the array from this direction.

In addition to the building compound there is an arroyo to the southwest that might also distort the wind flow. The mesquite bushes of the arroyo measure approximately 2 m in height and are slightly closer to the array than the compound, but have smaller aspect ratios of only 0.04. Again, they are not expected to exhibit much of an influence on the measurements but will also be filtered out of the analysis. More importantly, the arroyo is in the general direction of a large ridge spur of the Organ Mountains, from which significant drainage winds might be expected to originate during the evening period. Nonetheless, a sufficient supply of data not containing winds originating from this direction was found. It was thus possible to also filter out winds arriving from this quarter as well.

Other potential sources of wind field distortions are three data acquisition equipment enclosures that were located near the base of each tower. These were placed just behind the line of towers, as shown in figure 4. While each is less than a meter high, their position 12 ft behind the base of each tower provides one more reason to eliminate all winds arriving from the general direction of the 19472 compound.

To further characterize the terrain in the proximity of the tower array, a series of transit measurements were made to determine the slope of the terrain for wind flow calculation purposes. The transit was set up at the center of the tower array. Height readings were then taken in the directions 17° , 62° , 107° , 152° , 197° , 242° , 287° , and 332° relative to Magnetic North, which were the equivalent of looking along the array toward the north (at 17°), and then at intervals of every 45° thereafter. Height differences measured at these points relative to the central point were measured at 40 ft distant from the center in each direction. Measured height differences were -4.75 inches, -11.00 inches, -6.50 inches, -0.50 inches, +7.00 inches, +12.00 inches, +9.75 inches, and +6.25 inches, respectively. From these eight points, eight triangles were formed using the array center and two adjacent remote points. The two vectors extending from the center to two corners of each triangle define a plane and a normal vector. The (x,y) components of these eight vectors are plotted in figure 7a as red crosses.

Another common technique for determining the local terrain normal is based on analysis of the sensed winds themselves. To test the efficacy of this technique, a single two-day period in May was selected for a single sonic anemometer sensor. Over this period, 22 two-hour time periods were analyzed. In each two-hour period, 24 five-minute averaged 3D wind vectors were computed. These vectors were then fitted using a least-squares method to a plane that minimized the vertical offsets of mean wind vectors. Assuming that the prevailing wind flow is parallel to the terrain surface, the normal to this plane should then be equivalent to the terrain normal and thus indicate the terrain tilt magnitude and direction. The (06, 04) sensor was selected as a test case to determine the utility of this method for this data set. The resulting calculated normal vector direction cosines parallel to the tower line (M) and perpendicular to the tower plane (N) are plotted in figure 7 for each two-hour interval of the sample set. The wind analysis technique appears to fare poorly at inferring the appropriate terrain tilt compared to the direct survey measurement technique. This might be due to the fact that the dominant wind direction is from

the west during most time intervals, thus under representing wind vectors from the north or south that would reduce the least-squares error in the fitting plane calculation. Confidence in the wind vector approach is further diminished by its indication of a down slope direction that has an opposite sense compared to the measured surface tilt.

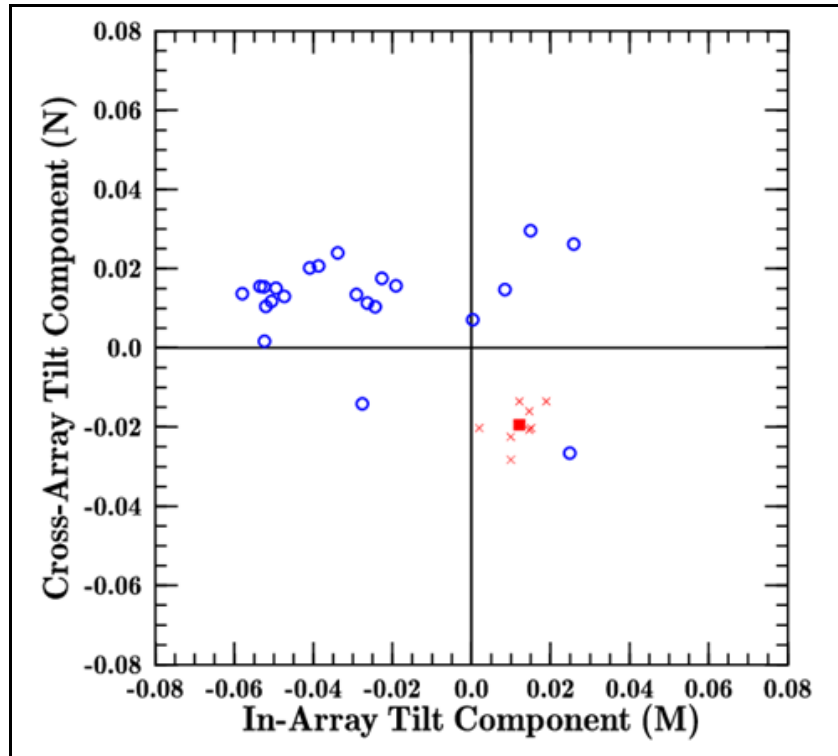


Figure 7. Terrain tilt calculations evaluated using two different methods.

Note: Red crosses indicate terrain tilt calculations based on surveyed measurements of surface height relative to a horizontal plane that contains a reference point within the array. The red box represents the centroid of eight of these tilt calculations, with a value of (+0.0121, -0.0194). Blue circles represent tilts determined from least-squares fits to 5-minute average wind vectors in 2-hour data sets from the (06, 04) tower sensor.

In addition to surveying the site itself, the positions of the sensor array were also measured using a triangulation technique. Readings were taken from two locations at either end of a 100 ft 10 inch baseline running roughly parallel to the 2D array at approximately 30 ft distance to produce sufficient parallax. The theodolite was 4 ft 9 inches above the ground surface at the pivot point. At each end of the baseline, the theodolite azimuth origin was set to True North before individual sensor measurements were taken. The direction to the opposing theodolite position was also measured. The northern theodolite position measured from the southern position was 21.08° Azimuth and -0.53° Elevation. Conversely, the southern theodolite position measured from the northern position was at 201.08° Azimuth, and 0.47° Elevation. Table 1 displays the reduced triangulation results rotated into a plane that has a minimum fluctuation in

the Y (perpendicular to the array plane) coordinate. The fitting operation essentially defined what we call “the array plane” that is required for further data analysis steps.

Table 1. Triangulated coordinates of array sensors rotated into a plane of minimal Y-Coordinate variation.

Sensor Name	X-Coordinate	Y-Coordinate	Z-Coordinate
(00,02) sonic	0.000000	0.000000	2.000000
(00,02) hygrometer	0.228713	0.047822	1.983979
(00,02) thermistor	0.608094	-0.002183	1.956546
(00,04) sonic	-0.019012	-0.001401	3.993020
(00,04) hygrometer	0.238167	-0.002704	4.023092
(00,04) thermistor	0.765711	-0.194896	3.975996
(00,06) sonic	-0.061285	0.013748	5.992137
(00,08) sonic	-0.081990	-0.031138	7.999926
(00,08) hygrometer	0.159137	0.030675	8.040467
(00,08) thermistor	0.503826	0.027353	8.008606
(00,12) sonic	-0.074926	0.040306	12.028629
(00,12) thermistor	0.463997	0.044818	12.049938
(04,02) sonic	4.058673	-0.016033	1.961009
(04,04) sonic	4.043249	-0.060248	3.999256
(04,08) sonic	4.007775	0.107220	8.024461
(06,02) sonic	6.084069	0.067915	1.991226
(06,04) sonic	6.051275	0.045842	3.985017
(06,06) sonic	6.072047	0.020140	5.993159
(06,08) sonic	6.040515	0.016420	8.011659
(08,02) sonic	8.093273	0.035163	1.997010
(08,04) sonic	8.089391	0.051620	3.995163
(08,06) sonic	8.068838	0.031854	6.022109
(08,08) sonic	8.043465	-0.029567	7.999169
(10,02) sonic	10.084801	0.010659	1.983814
(10,04) sonic	10.084266	0.019632	3.980428
(10,08) sonic	10.068114	-0.033071	8.012495
(14,02) sonic	14.120746	-0.018231	1.960489
(14,04) sonic	14.117549	-0.032374	3.984308
(14,06) sonic	14.134556	-0.003508	6.001172
(14,12) sonic	14.045970	0.129338	12.058891

X-coordinate and Z-coordinate data of sonic anemometer positions from table 1 are depicted graphically in figure 8 as 15 cm diameter blue circles centered on the projection of the measured position. Cardinal coordinates of perfectly positioned sensors are plotted in the same graph as red x's. It is apparent that the sensor positions are within close proximity of the centroid positions specified in the array design. The grid shows a systematic positioning drift that increases across the horizontal axis of the array relative to the reference point defined by the (00, 02) sensor position. It should be noted that the sensor head of the RM Young 81000 series sensors features a transceiver separation of approximately 6 inches or 15 cm. Evidently, the (x, z) separations between designed and actual sensor positions are comparable to the lateral extent of the measurement volume of an individual wind sensor. This positional error is much less than the nominal 2 m minimum separation of any sensor pair in the array and is therefore

inconsequential for wind azimuths within about $\pm 45^\circ$ range about the perpendicular to the array, even if we assume that all sensors are at their design positions in correlation calculations. Of course, we do have the option of improving the accuracy of any calculation (only marginally in most cases) by using the actual rather than design sensor position coordinates.

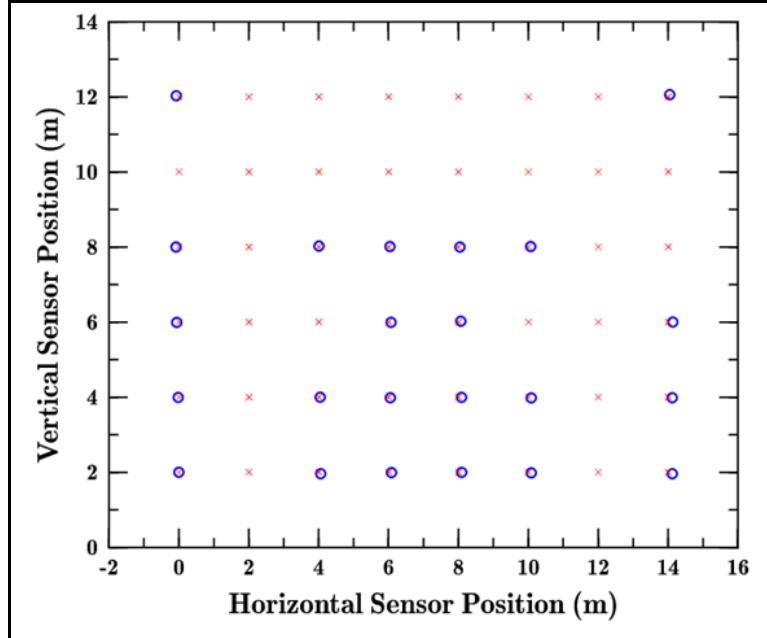


Figure 8. Graphical comparison between surveyed sonic anemometer locations and orthogonal 2 m position separations.

2.2 Data Acquisition and Handling

Data from the test were collected on Linux-based laptop computers. Each line of the data archive file was time stamped, and contained the three-component wind and temperature values measured by each sonic. The sonics were set to collect measurements at a 20 hertz (Hz) rate, as were the Li-Cor humidity sensors. The Li-Cor instruments logged their data into their own archive files, with a time stamp followed by measured absolute humidity and carbon dioxide (CO₂) concentration values. Groups of data records collected by each instrument were cached into the memory of the laptop, written to disk, and saved as hourly archive files. Each file name was automatically generated by the controlling system scripts and data collection software, and was designed to encode the sensor type, sensor location, day, month, and hour of the data collection. The temperature data from the six thermistors on or adjacent to the south tower and the radiative flux data from the Kipp-and-Zonen radiometer were assembled into an American Standard Code for Information Interchange (ASCII) record by a Campbell data logger. The output of this logger was recorded at a rate of $\frac{2}{3}$ Hz, somewhat faster than the expected time constants on the thermistors and the radiometer. The resulting hourly thermistor-radiometer data archive files were thus considerably smaller than the hourly sonic or Li-Cor archives, and used a similar file naming convention.

All sonic file names had an “SN” prefix; all hygrometer file names used an “LI” prefix; and all radiometer files began with “RT.” For example, the file “SN_0604_2008_04_10_0300.txt” is the sonic anemometer file associated with the 0604 location (6 m y position and 4 m z position) for data beginning at 0300 local time on April 10, 2008. The data file designations for the “LI” and “RT” files are slightly simplified in that they do not include the 4-digit location designator. In contrast, due to historical choices for sensor numbering in the data collection software, all the “RT” files are designated as “RT_01”, while the LI Li-Cor sensor files are designated as “LI_02”, “LI_03”, and “LI_04” for the 2 m, 4 m, and 8 m Li-Cor sensors, respectively. The logic behind these earlier designations is no longer relevant, but it seemed easier to maintain the convention than to modify the associated code.

3. Data Inventory

The measurement campaign commenced on April 9, 2008, and continued through June 14, 2008, covering two separate periods: April 9–30, and May 8–June 14. Our initial effort to characterize the data in this section will be limited to considering data quality, data consistency, and consideration of the range of mean conditions available. In the next section, the range of environmental stability conditions and characteristic properties of wind turbulence anisotropy will be considered. That is, unlike traditional laboratory experiments, one cannot control the environmental conditions present at any given moment in an atmospheric field experiment. Rather, one is typically limited to sampling a long series of data and seeking conditions that are congruent with the phenomenon of interest. This section describes that process.

3.1 Data availability

Our first task of the inventory phase, based on the section 2.1 discussion, is to identify and thereafter exclude periods when mean flow fields are arriving at the array from the east-southeast sector. Subsequent analysis can then focus on periods with winds arising from the northwest sector. In addition, we will identify periods when the ambient conditions match desired states of atmospheric stability, wind speed and directional consistency/uniformity. Unfortunately, in any real-world field experiment, sensors and data acquisition systems do experience malfunctions and failures from time to time. In our case, these disruptive events included high winds that knocked out local power and crashed the Li-Cor control electronics, the Campbell data loggers, and the laptop control/archive systems. Consequently, an initial analysis task is to screen the available data sets, excluding periods when any of the sensors went “off-line” (for any reason) from the analysis. Figure 9 is a graphical representation of sensor availability over the campaign period, and provides an easy means to filter out outage events.

Frequently, at least one sensor was unavailable due to an electrical problem. Fortunately, we appeared to retain the “fetch” tower data for virtually the entire test period. The best dates

appear to be Julian dates 109–112 and 150–164 when all sensors appeared to be available. The initial screened data inventory also includes a number of less-than-perfect periods where some sensors were not available, because we are looking for the widest practical range of weather conditions. The severity of sensor outages tended to vary. In some cases, a laptop simply “went down” at an unfortunate time and data collection from an entire tower ceased. For example, we lost the center tower’s laptop at 13:33 on April 10 under conditions where winds were gusting up to 30 m/s. This failure occurred long after the system had been checked on a day prior to a long weekend for the experimental team. The wind-induced power fluctuations disconnected the laptop’s data acquisition ports, a situation that was not corrected until the following Monday.

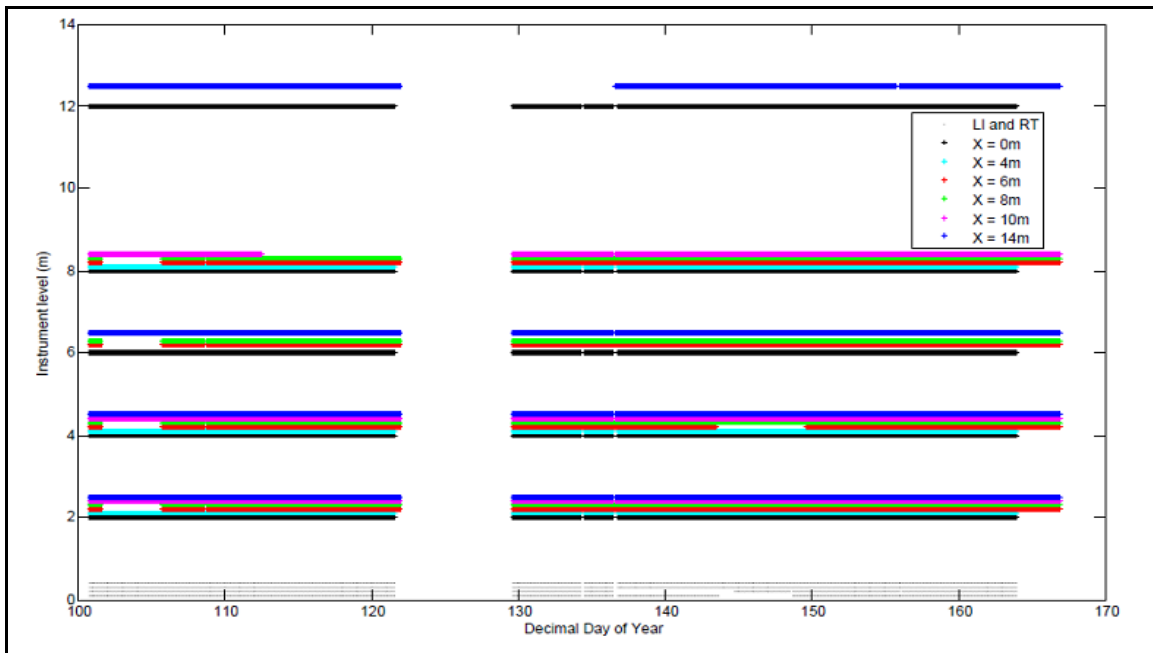


Figure 9. Graphical history of data availability during the measurement period.

Note: The vertical axis denotes the approximate elevation of a given sensor. The horizontal axis denotes time in Julian dates throughout the measurement period. The colors indicate the lateral (x) position of a sensor in the array. Li-Cor and radiometer data are plotted in gray at the bottom of the graph, with the traces representing the radiometer, 2 m, 4 m, and 8 m Li-Cors from bottom to top, respectively.

Thus, several days of data were lost for that tower. A shutdown after April 30 was even more severe, and required more time to bring systems back on line since the entire power grid to building 19472 had been damaged by winds. Despite these setbacks a large quantity of data were acquired over the 2+ month period of the experiment.

3.2 Wind speed statistics

Our initial analysis involves evaluation of mean hourly-averaged winds. Due to the similarity of the mean effects seen at each position within the array, the 4 m sonic sensor on the southern tower was selected as a suitable representative for the other array sensors. Figure 10 shows the

mean hourly winds and the streamwise and crosswind standard deviations from the mean observed during the period of the test.

Several features are apparent in this plot. The first is that the wind variances appear to have a relatively narrow range and that their magnitude does not generally correlate well to the mean wind. At times, the variances will be significantly less (percentage-wise) than the mean when the mean wind speed is high. Conversely, when the mean wind speed is low, the variances can be on the order of the mean wind. Secondly, figure 10 apparently indicates that the streamwise and crosswind standard deviations track one another and are of similar magnitudes at a given time, but this appearance is somewhat deceiving. Streamwise (green) and crosswind (red) standard deviations of winds about the mean direction are also plotted in figure 10.

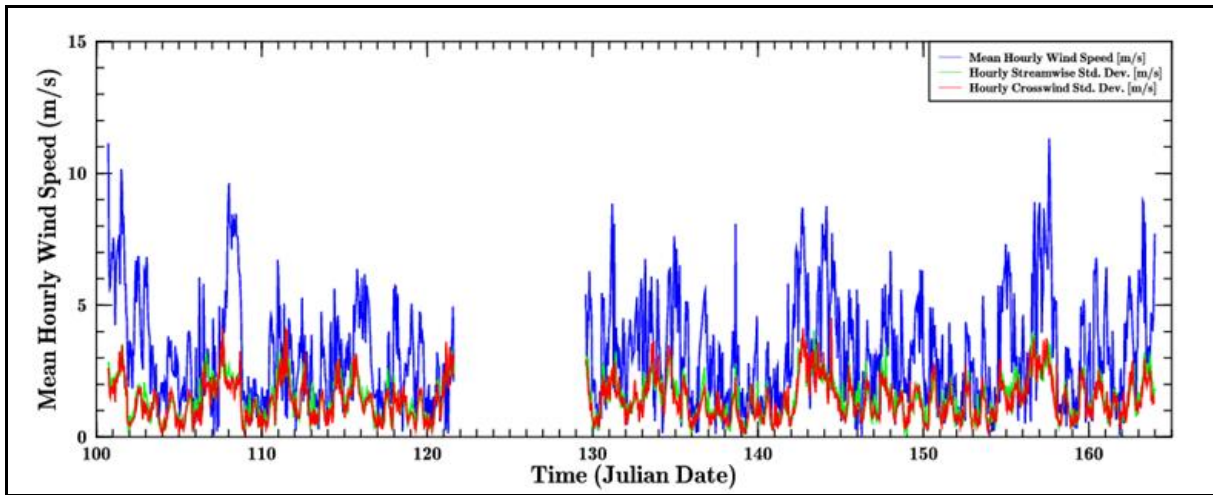


Figure 10. Graphical history of hourly mean wind speed (blue) observed during the test.

Figure 11 is a scatter plot of the standard deviations comparing streamwise and crosswind standard deviations by month of the test. Data points plotted represent hourly standard deviations. Data are discriminated according to calendar month of the test.

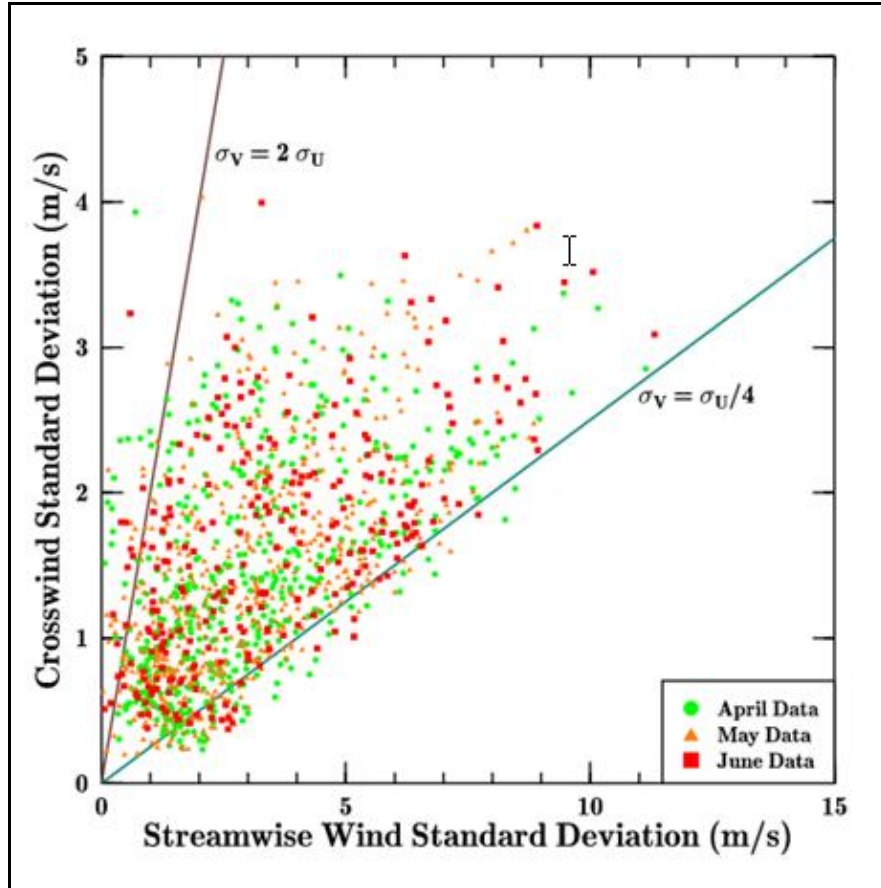


Figure 11. Scatter plot of streamwise versus crosswind standard deviations of wind speed about the mean wind vector.

This figure illustrates that the general wind statistics sensed throughout the testing period appear to be essentially stationary. Indeed, this was by design, as indicated earlier. It should also be noted that there were several strong wind events that occurred during the test, as well as a number of calmer periods.

3.3 Application of wind azimuth and speed filtration

In addition to the mean wind speed statistics, the mean wind azimuth had to be screened to select those cases where the observed azimuth was within the range of interest. In the following discussion, it should be noted that the sonic sensors were mounted so that a wind flowing in the -Y direction represents a wind that is perpendicular to the array, coming from the WNW.

The process of selecting those periods when the mean winds are directed from the proper quadrant may be illustrated with the aid of figure 12 (scatter plots a–c) that plot the hourly component winds for data taken during each month of the test period. Our selection criterion is that the mean wind direction should be within 45° of the ESE flow direction perpendicular to the array. The figure 12 scatter plots show a large number of cases where the winds pass through the array in the “wrong” direction.

A second filtering criterion involved the consistency of the mean wind. Cases where the streamwise standard deviation was larger than the mean wind speed were also removed. A third criterion involved the requirement that data from all three towers be present. On at least five occasions at least one whole tower's data were lost.

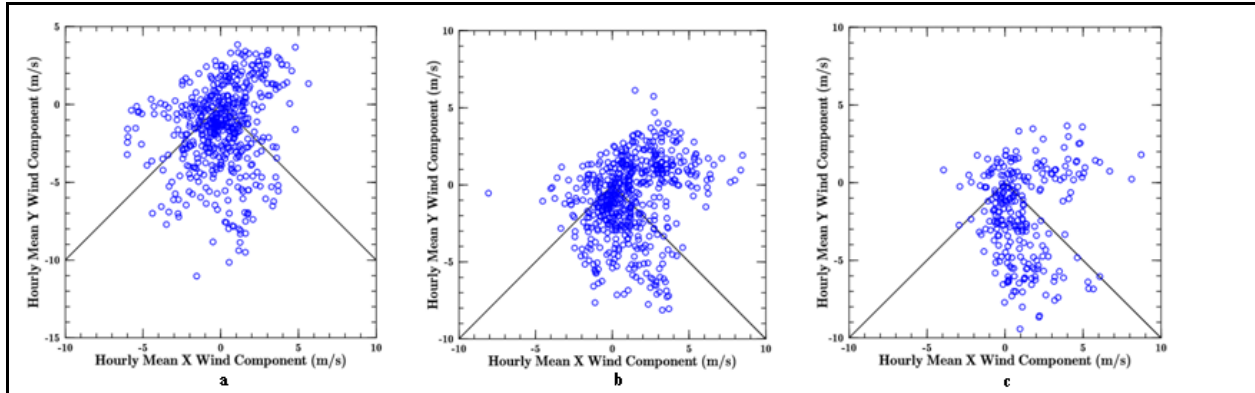


Figure 12. Scatter plots a, b, and c of X and Y hourly averaged mean wind components during each month of the test period (April to left and June to right).

Note: Demarcation lines indicate azimuth acceptance criteria for further study of the data. X and Y axes both range from -10 m/s to +10 m/s, except in scatter plot a where the $-15 \text{ m/s} < Y < +5 \text{ m/s}$.

Only those periods were considered where there were at least two consecutive hours that simultaneously satisfied all of the aforementioned criteria. This enhanced consistency requirement ensures that marginal conditions can be removed. The filtered data are then evaluated for flux and correlation statistics. The filtration process is illustrated graphically in figure 13. The purple dots represent hourly mean wind speed data that match all of the described criteria.

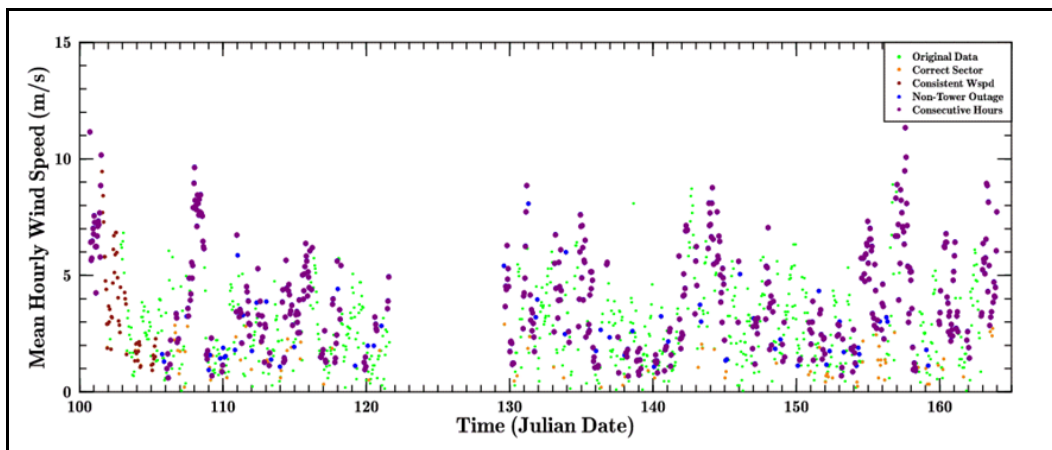


Figure 13. Filtered hourly data sets selecting out hours according to increasingly discriminating criteria.

Note: Original data are green; orange indicate conditions falling within the proper wind azimuth sector, brick red indicate those with mean wind speed greater than the streamwise wind standard deviation, blue indicate all towers functioning, purple indicate at least two consecutive hours matching all prior criteria.

Although numerous data were rejected through this selection process, 470 hours of data survived the editing process, and appear to provide a representative sample of the weather conditions and winds observed. We note that virtually all of the orange dots (acceptable wind azimuth, unacceptably large fractional streamwise speed variance) are at low wind speeds. This was likely due to “light and variable” wind conditions that often prevail. Such winds would not, however, be useful in a study of this type, since our focus is on correlated fluctuations between horizontally spaced sensors when the wind can be clearly characterized as following a given trajectory. Light and variable winds necessarily imply that the wind field trajectory is inconsistent and would be poorly characterized by our subsequent analysis techniques.

3.4 Stability and ambient temperature considerations

Although figure 13 is useful in accumulating a body of data that satisfy the selected criteria, a separate concern is whether or not this pool of data provides a representative and diverse range of wind and stability conditions that can be tested for correlations. To better judge this aspect of the data set, instead of plotting the time dimension in terms of the decimal Julian date, the data can be plotted only as a function of the time of day. This is shown for just the fully filtered group of selected data in figure 14.

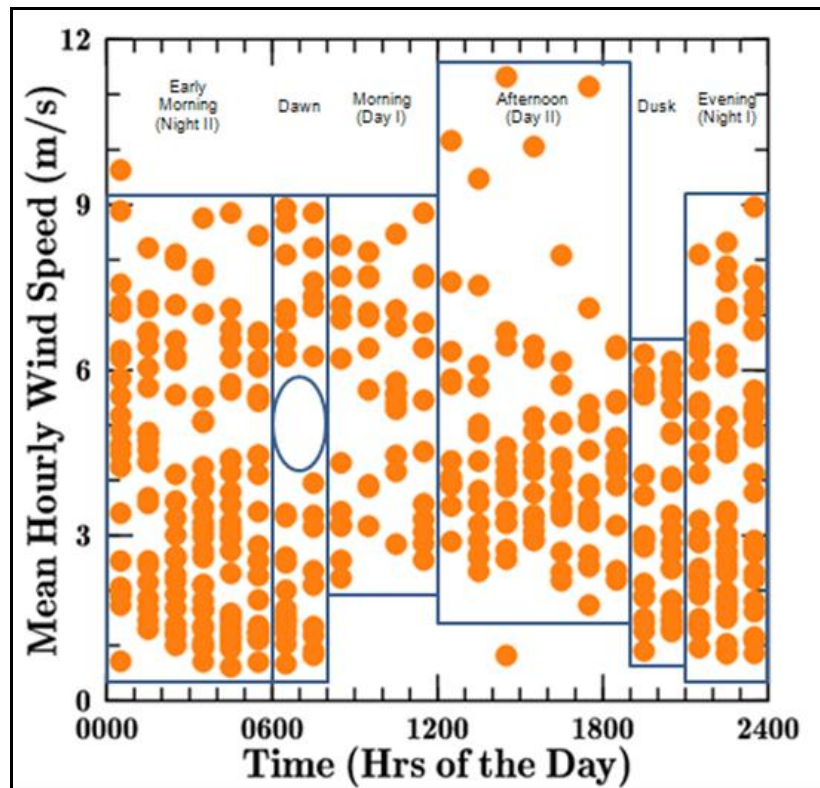


Figure 14. Mean hourly wind speeds plotted relative to time of day to show available wind versus time states available.

Note: The diurnal cycle has also been subdivided into potential state distribution subclasses.

Some correlation exists between time of day and atmospheric stability condition, so that one may infer that during nighttime periods it is more likely to encounter stable conditions than at other times. Similarly, during the daytime unstable conditions are expected. Figure 14 indicates that our selected set of wind speed data should indeed cover a wide range of conditions. Note, however, that significant gaps exist in the set that are apparently systematic. Two obvious gaps exist for very low wind speeds during daylight hours between 0900 and 1900 and intermediate wind speeds between 4 and 6 m/s in the post-dawn period 0600–0900. The latter of these two gaps may be associated with a selection artifact due to terrain-induced drainage winds. For the other apparent gap, the scarcity of low-speed winds in the daytime data set is most likely due to routine convective coupling of the planetary boundary layer with upper level high speed winds that is a normal springtime occurrence at WSMR. It is apparently important to associate stability conditions with specific members of the filtered data set. As is obvious when comparing the data plotted in figure 14 with the dynamical plot indicated in figure 13, to merely have a range of sampled wind conditions is useful, but it is likely that a particular wind condition will correlate with specific stability states. Hence, figure 14 illustrates the need for the application of further classification criteria to each hourly data set.

In the absence of detailed atmospheric profile data (for heights well above the 3DTS Test array) that may be used to objectively evaluate stability and wind field turbulence at each data point, we must resort to other approaches to correlate our wind data with stability. Following our observation discussed previously, one alternative is to group the data by local time windows and to associate a probable stability state with each data set window. Of course, in the cases of stable and unstable conditions, the wind data would be distributed over a range of stability strength. For example, it appears reasonable to assume that the conditions observed between approximately 1200 and 1800 are representative samples within a single distribution of unstable states. Likewise, the winds between the 1900–2200 and 2200–0600 periods exhibit different distributions over stable states. The 0600–0800 period is a near neutral early heating period. The 0800–1200 window represents a convection buildup period, but with smaller scale wind coupling than the afternoon period (during which convective flow effects due to general motions within the deep convective layer that sets up over the WSMR area and can often measure up to 3 km in depth). The sunset timeframe of 1800–1900, containing the evening neutral event, does not experience the wind speed lows of the 1900–2200 period, it also does not experience the same high winds as the afternoon period.

Though these speculations are perhaps useful qualitatively, they are probably quantitatively insufficient for our purposes. Their chief utility lies in pointing out that there are real similarities in the plotted wind distributions in these different time segments. Therefore, it would appear realistic to consider evaluating the stability versus mean wind conditions present in each of these segments using some objective measurement approach. Before proceeding to this task, however, a final discussion of the mean effects will be considered.

Another mean parameter that needs to be analyzed over the 3DTS experiment period is the hourly temperatures that are measured by the sonic sensor. Experience shows that the absolute calibration of sonic anemometer temperatures is not truly accurate. However, an individual sonic sensor can provide a reliable relative measure of long-term (diurnal and seasonal) temperature variations. An example of such data is plotted in figure 15.

These data display the obvious increasing seasonal temperature trend throughout the measurement period. It is also of interest to compare variations in temperature (primarily cooling episodes) associated with high wind events. The wind event on Julian date (JD) 108 was accompanied by a steep drop in mean temperature, indicating a cold frontal passage. Wind events recorded on dates JD 142–145 and JD 157 exhibited similar behaviors.

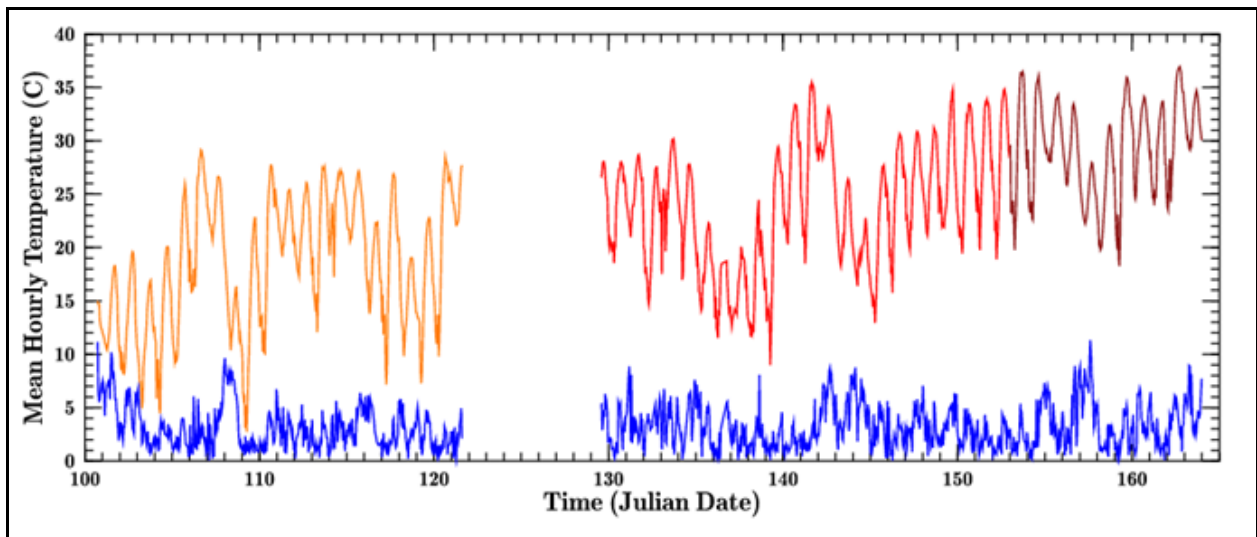


Figure 15. Mean hourly temperature values sensed by the 4m flux profile sensor during the experimental measurement period (orange equals April, red equals May, brick red equals June).

Note: Also plotted are the mean hourly winds sensed (m/s).

Overall, over 350 hours of data qualified for further analysis under our selection criteria. It is therefore expected that this data set will be a significant and useful resource for future analytic exploration.

4. Analysis of Stability and Anisotropy Conditions Observed

An analysis of 2D structures in wind flow turbulence is facilitated by correlation of anisotropy with atmospheric stability. Thus, it is of interest to simultaneously quantify the degree of stability or instability in the boundary layer as well as the degree of anisotropy in the flow field turbulence. We identify useful stability and anisotropy parameters below that may be constructed from the meteorological observables. A brief discussion of how these parameters interplay under measured field conditions closes out this section.

4.1 Stability metrics

To quantify the stability, it is beneficial to develop a temporally consistent measure, so that periods of either highly unstable or highly stable conditions can easily be identified for further study. Traditionally, the Monin-Obukhov length provides this stability parameter, representing a height scale at which buoyant turbulence overtakes mechanical turbulence as the dominant energy production mechanism. However, previous and current experiences with Obukhov lengths calculated from available field data demonstrate that the results frequently vary abruptly over short time scales, a trait that we do not expect in the temporal variation of stability. Obukhov length variations are particularly large under light-and-variable wind conditions.

Consequently, an alternative to the Obukhov length stability metric was sought. The best alternative appeared to be simply the measured near-surface vertical temperature gradient. Although this quantity is also highly variable at the highest temporal resolutions, it nevertheless provides a consistent indicator of the buoyancy when a longer-term mean is computed. To generate this parameter, the thermistor temperature measurements were fitted to the function $T = A \ln(z) + B$ via a least-squares technique. The temperature gradient for any given height and time is then given by $dT/dz = A/z$. Figure 16 plots gradient results obtained during April 2008.

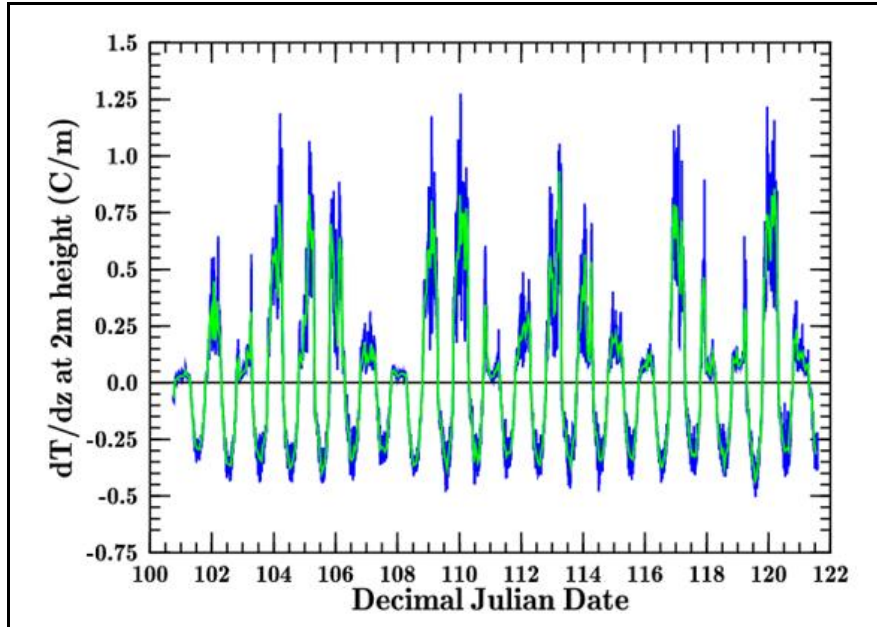


Figure 16. Least squares computed mean vertical temperature gradients (C/m) at 2 m height for April. Blue line: 1-minute average results. Green line: 1/2-hour averaged 1-minute results.

The daytime gradients appear consistent in their temporal behavior, but nocturnal gradients markedly vary in response to high wind speed mixing effects. Similar May and June results are shown in figures 17 and 18.

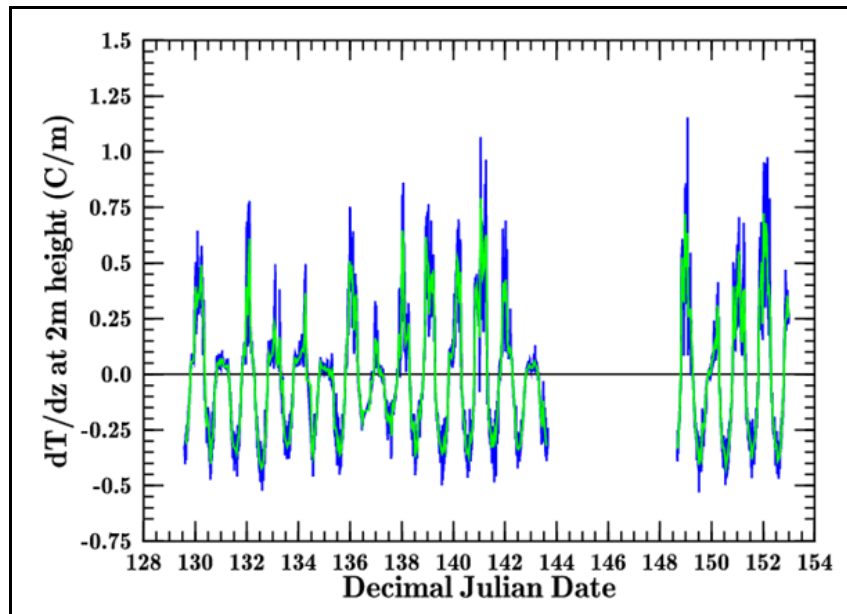


Figure 17. Least squares computed mean vertical temperature gradients (C/m) at 2 m height for May. Blue line: 1-minute average results. Green line: 1/2-hour averaged 1-minute results.

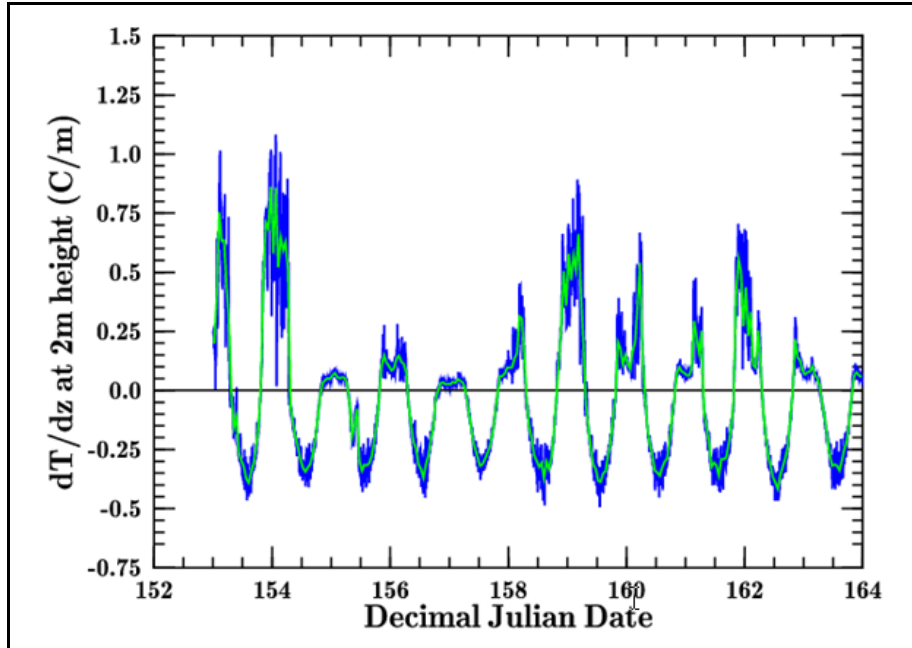


Figure 18. Least squares computed mean vertical temperature gradients (C/m) at 2 m height for June. Blue line: 1-minute average results. Green line: 1/2-hour averaged 1-minute results.

The influence of nocturnal winds on the inversion strength is a well-known phenomenon, so the large variability in our nocturnal gradients in figures 16–18 suggested that we take a closer look at our data. Figure 19 examines this influence in the form of a scatter plot of April gradients versus ambient mean wind speed.

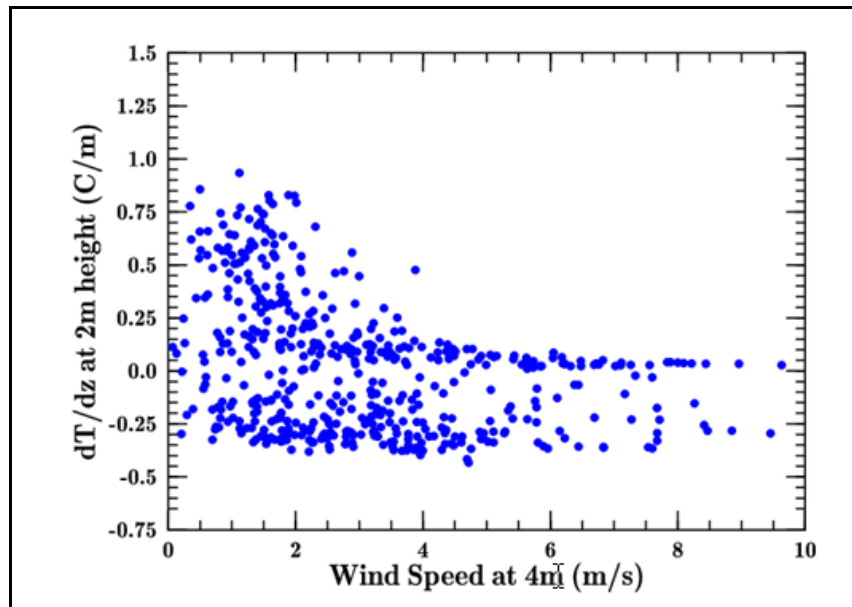


Figure 19. Scatter plot of measured hourly mean horizontal winds at 4 m and estimated mean vertical temperature gradients at a 2 m height calculated from least-squares analysis ($A/2$ from the least squares analysis).

Note the presence in figure 19 of negative daytime temperature gradients at high wind speeds that are comparable to the daytime minima of figure 16. It is thus clear that the daytime gradient is at most only weakly affected by the mean wind speed. Conversely, the figure 19 scatter plot illustrates the clear fragility of nocturnal inversion strength to the influence of even moderate winds. An obvious decay in temperature gradient occurs for wind speeds above approximately 2 m/s. Strong inversion conditions (+0.25 K/m – +0.75 K/m) can exist for winds below 2 m/s, but are virtually unattainable for wind speeds greater than 4 m/s.

It should be emphasized that the spring timeframe was selected for this experiment based on the climatological expectation of strong mean winds. Thus, strong inversion conditions were not specifically sought. If they had been preferred, the fall season would have been selected. Hence, only a seasonally representative set of inversion conditions was observed, not a comprehensive set that could only be obtained from a continuous multi-year experiment. Even so, a consistent observation is that one cannot find, simultaneously, both strong winds and highly stable conditions. The two are effectively mutually exclusive, since the winds tend to mix the vertical stratification. The effect is well known, and illustrated graphically in figure 19, but is implicit in the figure 14 analysis categorizations.

It is also well known that atmospheric turbulence effects follow a fractal $-5/3$ power law for the inertial subrange portion of observed fluctuation spectra. In most cases those spectra are constructed simply by converting data time series to spectral form by performing a one-dimensional (1D) time-based Fast Fourier Transform (FFT) on the data. The problem with this approach is that it assumes the turbulent fluctuations are isotropic. However, we know that often the data being transformed contain both 2D anisotropic as well as 3D isotropic fluctuations. How do we elicit evidence for 2D or 3D structure from our data sets?

Several avenues of analysis present themselves to uncover such structure. One that is specifically supported by the current test is point-to-point correlations between transverse points in the 2D array. However, analysis techniques based on the analysis of the Reynolds stress tensor of a single sensor also support the possibility of identifying specific anisotropic characteristics of winds detected by a single sensor.

4.2 Anisotropy metrics

Lumley (1978) developed an analysis technique for describing the amount of 2D fluctuations in a flow based on evaluating a parameter, F that is constructed from elements of the Reynolds stress tensor. Lumley's method was then expanded by Choi and Lumley (2001), and can be studied at multiple scales using a method adapted from Howell and Mahrt (1997) based on the Haar transform.

Lumley's analysis of the structural content of turbulence was primarily motivated by his interest in the return to isotropy of anisotropic flow. Using invariant parameters I_1 , I_2 , and I_3 (derived

from the Reynolds stress tensor and defined below), he developed the invariant parameter F (Choi and Lumley, 2001)

$$F = 1 + 9 I_2 + 27 I_3 \quad (1)$$

that exhibits the property that $F = 1$ when isotropic wind fluctuation conditions are present, and $F = 0$ represents conditions where significant 2D or 1D turbulence anisotropies are present.

The definition of the F parameter starts with the definition of the Reynolds stress tensor. This tensor \mathbf{R} consists of the nine elements that are wind fluctuation variances and covariances averaged over a particular time period:

$$\mathbf{R}_{ik} = \overline{u_i u_k}, \quad (i = 1 \dots 3, k = 1 \dots 3) \quad (2)$$

where the u_i represent instantaneous wind fluctuations relative to the mean wind component along the i th coordinate axis. We note that the $i = 1$ direction is traditionally along the mean wind axis while the $i = 3$ axis is generally in the direction perpendicular to the local ground surface although the invariants are independent of coordinate system choice. Because the fluctuations of the three Cartesian wind components about their respective means are unsigned scalars, their mean products commute, so that this tensor is symmetric, such that there are only six free parameters, not nine. Choi and Lumley (2001) created a new dimensionless and zero trace variant of the Reynolds stress tensor, termed the ‘‘anisotropy tensor,’’ with the following elements:

$$b_{ik} = \frac{\overline{u_i u_k}}{q^2} - \frac{\delta_{ik}}{3}, \quad (3)$$

where

$$\overline{q^2} = \text{Trace}(\mathbf{R}) = \sum_{i=1}^3 \overline{u_i u_i} \quad (4)$$

is the trace of the Reynolds stress tensor and δ_{ik} is the Kronecker delta function. Note also that the trace given in equation 4 is twice the mean kinetic energy density of the fluctuations. One can then define quantities $I_1, I_2,$ and I_3 as invariants of this tensor. The first of these invariants (I_1) is the trace of the anisotropy tensor, which by virtue of equations 3 and 4 is always zero by definition. The second and third invariants represent a binary product summation and a triple product sum akin to the determinant:

$$I_2 = -\frac{1}{2} \sum_{i=1}^3 \sum_{k=1}^3 b_{ik} b_{ki}, \quad I_3 = \frac{1}{3} \sum_{i=1}^3 \sum_{k=1}^3 b_{ik} \sum_{m=1}^3 b_{km} b_{mi} \quad (5)$$

Insight into the spatio-temporal structure of 2D versus 3D flow can be obtained by varying the averaging period for evaluations of these invariants. Thus, Lumley’s parameter F can be cast as

a function of the averaging time, or by implication, a flow-length scale that is proportional to the product of the averaging time and the mean wind speed. Typical averaging times for propagation characterization studies range from several minutes (Consortini et al., 2002) to 30–60 minutes (Andreas et al., 2003), depending on the variable to be measured.

4.3 Correlation of anisotropy with stability and other parameters

As an example of the significance of the flow-length scale, data collected during the Joint Urban 2003 experiment (JU2003), conducted at Oklahoma City, OK, in 2003, were analyzed by computing the parameter F using a variable averaging interval, examining both daytime and nocturnal cases. Figure 20 plots the values of parameter F as a function of the length scale inferred from the product of the averaging time and mean wind speed. These results clearly show that F undergoes a transition between fully 3D turbulence at scales less than 10 m to fully 2D turbulence at scales greater than 1 km. Comparison between the two plots indicates a similar spatial transition during daytime and nighttime conditions, although the nocturnal data show greater dispersion of the relation. However, note that analysis at larger length scales requires longer data sets, leading to the influence of non-stationary factors such as variable cloud cover, solar radiation, and/or synoptic changes in the mean wind speed or direction.

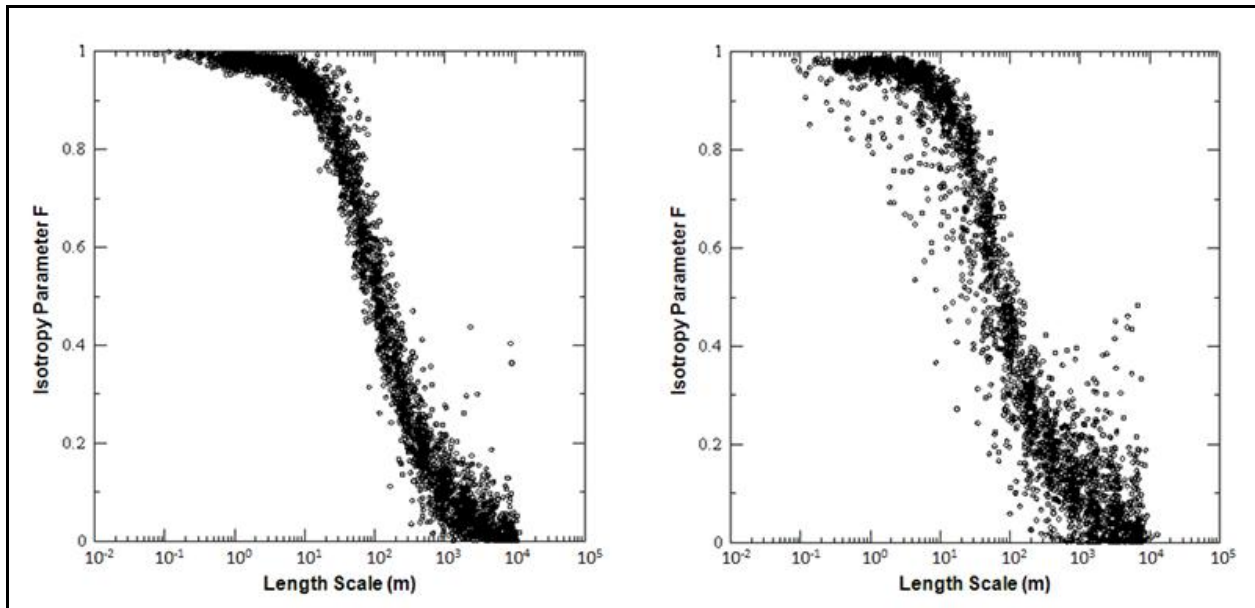


Figure 20. Isotropy parameter F as a function of length scale for day (left) and night (right) cases based on data collected at the 10 m level.

One can also apply a threshold to the F parameter as a means of qualifying a given turbulent wind field as isotropic or anisotropic. The flow-length scale at which the transition occurs will vary with time and atmospheric state, and should be diagnostic of the size of anisotropic features. For example, selecting a threshold F value of 0.9, one can study the length associated with this transitional value as a function of time throughout a diurnal cycle. At each point T in time, a Hanning temporal weighting window (with full-width half-maximum [FWHM] of ΔT) is applied

to averaging of the wind component fluctuations. We vary this averaging time ΔT and compute $F(\Delta T)$ from the averaged fluctuations for each ΔT . This process eventually identifies a $\Delta T_{0.9}$, so that $F(\Delta T_{0.9}) = 0.9$. An associated flow-length scale is then computed as $L_f = U \Delta T_{0.9}$ based on the associated mean horizontal wind speed U , computed using the same time-averaging interval. Figure 21 shows an example of such calculations based on data collected on June 10, 2007 using 6 RM Young sonic anemometers in the same area used for the 3DTS test. These sensors were set up side-by-side for intercomparison purposes in a pre-test check of sensors for the Boundary Layer Turbulence (BLT) test, a precursor test to the 3DTS.

Another means of considering the anisotropic information associated with a single sensor is through a direct analysis of the eigenvalues and eigenvectors associated with the Reynolds stress tensor. The eigenvalues for isotropic turbulence would be expected to be equal in each cardinal direction. However, such behavior is never found when considering stress tensors close to the earth's surface. Rather, it is common to find the three eigenvalues of the stress tensor to exhibit three distinct values that are positive definite.

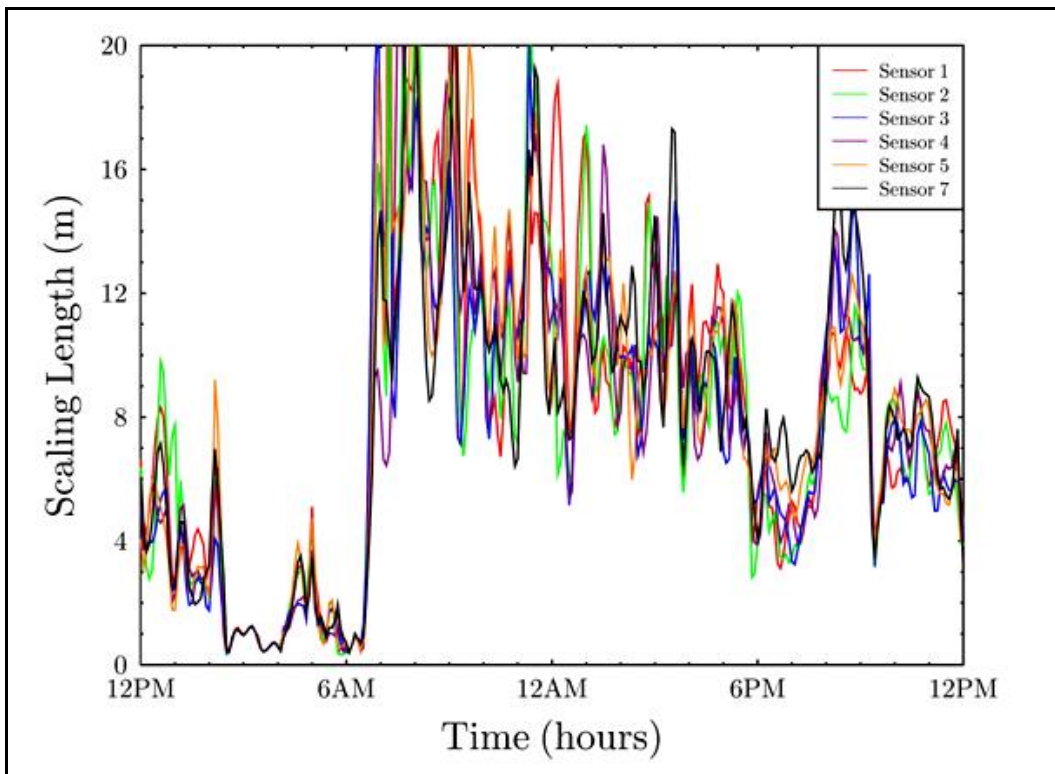


Figure 21. Diurnal dependence of L_F length scale for 10 Jun 07 intercomparison data.

Moreover, the eigenvectors associated with the two largest eigenvalues will always be oriented approximately in the horizontal plane. Second, and surprisingly, the eigenvector associated with the largest eigenvalue is commonly not oriented in the direction of the mean wind. Instead, the major eigenvector is often distributed about the horizontally transverse direction. The Reynolds stress tensor can thus be envisioned in the form of a flattened ellipsoid whose principal axes are identified by the eigenvectors and whose dimensions along the main ellipsoid directions are

proportional to the eigenvalues. The main eigenvector can be identified based on its proximity to the mean wind direction. The “second” eigenvector will then be approximately in the horizontal plane as well, while the “third” eigenvector will be primarily oriented in the vertical direction but will exhibit a forward-directed tilt into the mean wind direction (due to the influence of the mean momentum flux directed toward the ground).

To characterize these average effects, figure 22 first illustrates a scatter graph comparing the magnitudes of the first and second largest eigenvalues of the Reynolds stress tensor (which is also sometimes called the “Turbulent Kinetic Energy” [TKE] tensor). The graph illustrates that the 3DTS site appears to have a relatively consistent (characteristic) ratio between the largest and second largest eigenvalues.

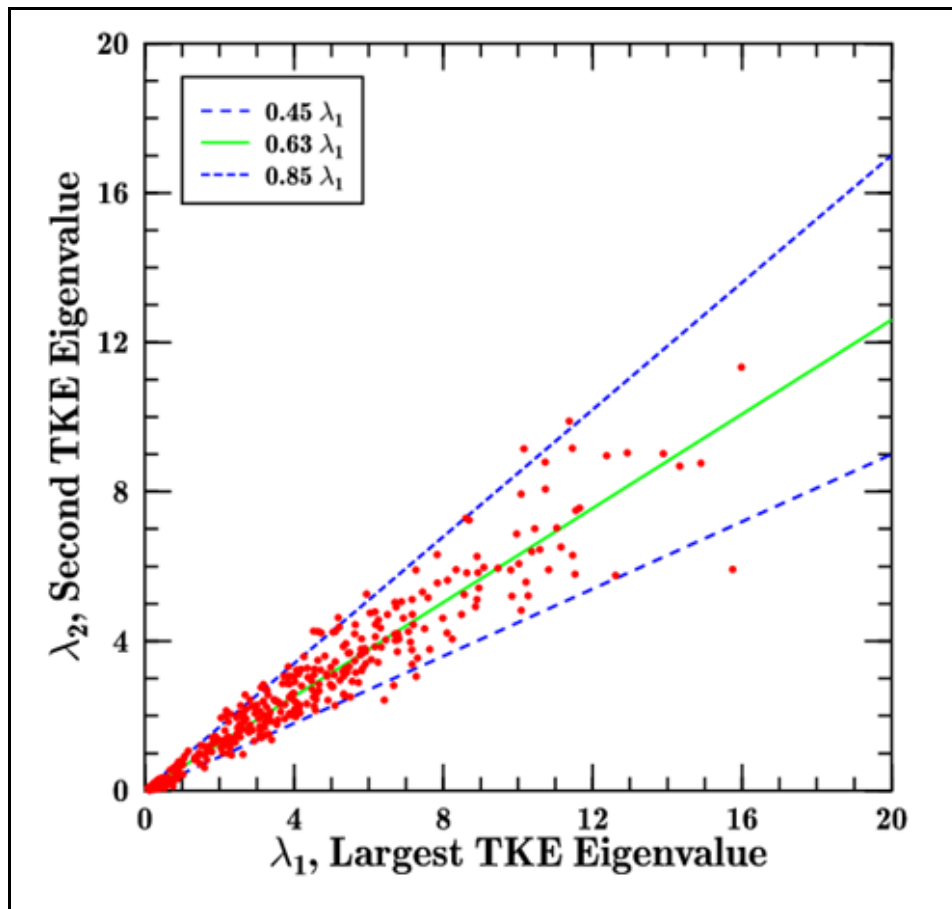


Figure 22: Scatter graph of the first and second largest TKE eigenvalues.

Having identified a fairly consistent “characteristic ratio” of the first to second eigenvalues of 1.00:0.63, or approximately 3:2 or 5:3, with approximately +/-30% scatter about the mean, we next consider the distribution of the azimuth of the main eigenvector relative to the mean wind vector in figure 23. In this figure, the zero degree angle was considered the center of the plot because it was anticipated that the along-wind direction would be associated with the largest TKE ellipsoid component. Yet surprisingly, the principal vector for the 2D-SAT data set is

oriented within approximately 30° of the transverse (crosswind) axis rather than the downwind (x or u) axis. Further analysis will be needed to fully explain this result, and a further differentiation of this parameter under varying stability conditions is likely necessary to ensure that stability dependent effects exhibiting different traits are not being aggregated.

Finally, in figure 24 we consider the angular projection of the third eigenvector relative to the vertical axis in the direction of the mean wind is considered. A “rule of thumb” in research circles indicates this projection angle should be approximately 17° under neutral stability conditions. The data plotted for the site again aggregates all stability conditions for the (06, 04) sensor, chosen because of its proximity to the center of the array. The data indicate a distribution whose mean value is $\sim 8^\circ$ with a full-width half-maximum range between 4 and 14° .

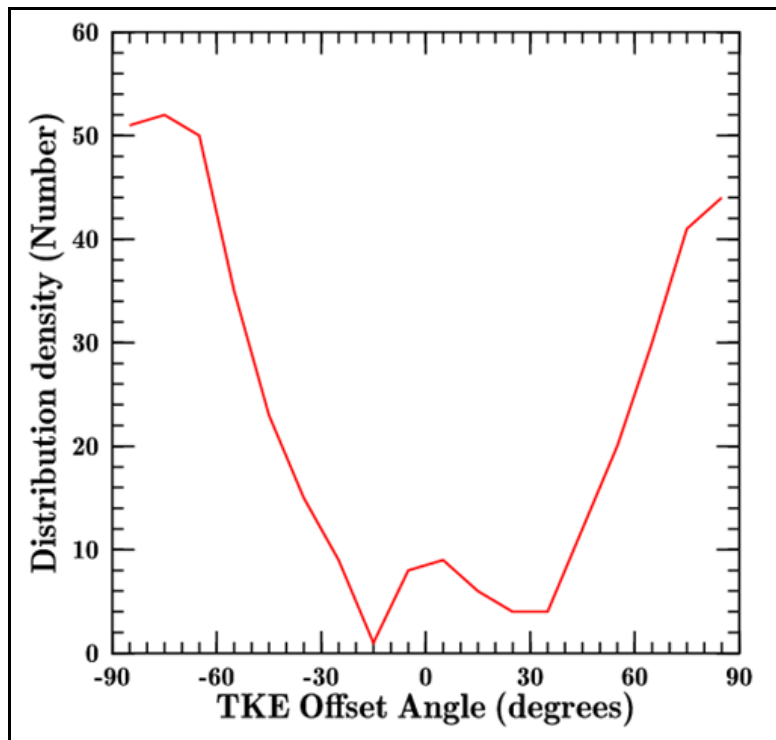


Figure 23. Probability distribution of the angle created between the mean wind direction and the principal eigenvector of the TKE ellipsoid.

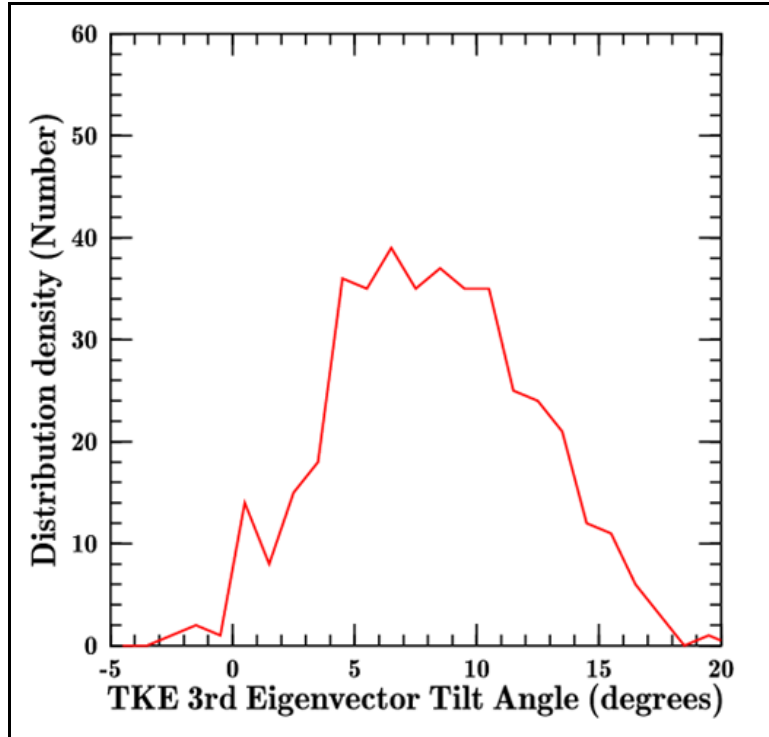


Figure 24. Distribution plot of the angle between the projection of the third eigenvector onto the mean wind axis and then determining the angle between this projection and the vertical axis.

5. Conclusions

This first report on the 3DTS Test has described the scope and purpose of the measurement program conducted in the spring of 2008. One major finding is that this is a robust data set that captures a wide range of conditions, meeting our primary objective of developing a data set suitable for understanding a variety of turbulence effects in the atmospheric surface layer. Preliminary analysis of the Reynolds stress tensor eigenvalues indicates general agreement with results from other data sets. However, the nearly 90° angle between the mean wind direction and the direction of the eigenvector associated with the largest eigenvalue is a significant difference from findings using neutrally stratified laboratory flows. This discrepancy may be one reason laboratory flows do not always capture atmospheric phenomena.

There are many more data analysis experiments to be done with this data. An initial motivation for this experiment was to investigate more deeply the problematic Fourier spectra encountered at RTG-40. Repeating that analysis using this data is a top priority for future data analysis. However, the Army impact of understanding the connections between turbulence strength, structure, and anisotropy goes beyond RTG-40. It influences how and to what extent turbulence affects passive and active imaging systems and lasers operating near the Earth's surface. It also

affects the coupling used in models to describe surface fluxes of energy that are incorporated into more general weather prediction models, the connection between turbulence and coherent structures in the boundary layer, and wind drag effects.

The unique 3D volumetric nature of the data allows full (TKE) budgets to be conducted. Previous TKE budget studies have only been two dimensional, where the usual single tower data has been used with the assumption of horizontal homogeneity. The 3DTS data will allow us to determine when that assumption holds and under what conditions it does not. Knowing this over open terrain will then help in extrapolating to complex terrain, such as urban or forest, where the surface is horizontally inhomogeneous, much more typical of modern battlespaces. In addition, we hope to analyze the data to see if we have captured large scale coherent events, such as dust devils or horizontal roll vortices, passing through the array. These events may be responsible for a disproportionately large fraction of transport. They are also inherently two dimensional in nature and will have a profound impact on the isotropy of the turbulence. Being able to determine the frequency and magnitude of such events will be useful for modeling transport, dispersion and the resuspension of previously deposited material. The 3DTS data can also be used in anisotropy studies to relate the anisotropy at a single sensor to other sensors at varying separations. The study of turbulence anisotropy is still new and addresses the fundamental assumptions of current theories. Also, a key measure of correlations at increasing distances is the structure function. In an anisotropic setting this function becomes not merely a function of increasing distance but also a function of direction, turbulence state, height, and stability. To this we can add the outer scale of turbulence, though this parameter is likely a function of the prior list. We also expect that the turbulence condition present will provide a measure of the means of distinguishing properties of two-dimensional and three-dimensional turbulence.

This overview and the initial analysis results are necessarily introductory as the primary purpose of this report is to set the stage for future reports that consider details mentioned above of the measurements taken.

6. References

- Andreas, E. L.; Fairall, C. W.; Persson, P. O. G.; Guest, P. S. *Probability Distributions for the Refractive Index Structure Parameter and the Inner Scale of Turbulence and Their Implications for Flux Averaging*; TR-03-24; ERDC/CRREL: Hannover, NH, 2003.
- Choi, K.-S.; Lumley J. L. The return to isotropy of homogeneous turbulence. *J. Fluid Mech* **2001**, 436, 59–84.
- Consortini, A.; Innocenti, C.; Paoli, G. Estimate method for outer scale of atmospheric turbulence. *Opt. Comm.* **2002**, 214, 9–14.
- Hill, R. J. Corrections to Taylor’s frozen turbulence approximation. *Atmospheric Research*, **1996**, 40, 153–175.
- Horst, T. W.; Kleissl, J.; Lenschow, D. H.; Meneveau, C.; Moeng, C.-H.; Parlange, M. B.; Sullivan, P. P.; Weil, J. C. HATS: Field Observations to Obtain Spatially Filtered Turbulence Fields from Crosswind Arrays of Sonic Anemometers in the Atmospheric Surface Layer. *J. Atmos. Sci.* **2004**, 61, 1566–1581.
- Howell, J. F.; Mahrt, L. Multiresolution flux decomposition. *Boundary-Layer Meteorology* **1997**, 83, 117–137.
- Kaimal, J. C.; Wyngaard, J. C.; Izumi, Y.; Cot’e, O. R. Spectral Characteristics of Surface-Layer Turbulence. *Q. J. Roy. Met. Soc.* **1972**, 98, 563–589.
- Kolmogorov, A. N. The local structure of turbulence in incompressible viscous fluid for very large Reynolds numbers. *Proc. USSR Acad. Sci.* **1941**, 30, 299–303.
- Lumley, J. L. Computational Modeling of Turbulent Flows. *Adv. in Appl. Mech.* **1978**, 18, 123–176, Academic Press.
- Sullivan, P. P.; Horst, T. W.; Lenschow, D. H.; Moeng, C.-H.; Weil, J. C. Structure of subfilter-scale fluxes in the atmospheric surface layer with application to large-eddy simulation modeling. *J. Fluid Mech.* **2003**, 482, 101–139.
- Tofsted, D. H. *Turbulence Simulation: Outer Scale Effects on the Refractive Index Spectrum*; ARL-TR-348; U.S. Army Research Laboratory: White Sands Missile Range, NM, 2000.
- Tofsted, D. H.; Quintis, D.; O’Brien, S.; Yarbrough, J.; Bustillos, M.; Vaucher, G. T. *Test Report on the November 2005 NATO RTG-40 Active Imager Land Field Trials*; ARL-TR-4010; U.S. Army Research Laboratory: White Sands Missile Range, NM, 2006.
- Tofsted, D. H.; O’Brien, S.; Klipp, C. The Presence of Two-Dimensional and Three-Dimensional Turbulence in the Near-Earth Atmosphere; *Eos Trans. AGU*, 88(52), *Fall Meet. Suppl.*; Abstract U43B-1135 (2007).

Tong, C.; Wyngaard, J.C.; Khanna, S.; Brasseur, J.G. Resolvable-and subgrid-scale measurement in the atmospheric surface layer: Technique and issues. *J. Atmos. Sci.* **1998**, *55*, 3114–3126.

INTENTIONALLY LEFT BLANK.

Appendix. Tower Construction Images

The photographs in this appendix were selected to show the participants in the construction of the 2D array and to provide some sense of the scope of the construction task as well as the progress and steps required to complete this task.



Figure A-1. Scott Elliott holds sonic with its data/power pigtail, with Sean O'Brien and Edward Creegan by 40 ft tower.



Figure A-2. David Tofsted, Robert Brice, and Scott Elliot inspect mounting bracket on tower boom.



Figure A-3. Cross bracing system shown on mounted tower.



Figure A-4. Detailed view of mounting method for sonic anemometer, hygrometer and thermistor on flux profile boom.

Note: Green arrow identifies cross brace attachment screw. Red arrows identify cross braces for boom stabilization.



Figure A-5. Fully wired and instrumented flux profile tower awaits setup.

Note: Sawhorses are staked to ground to avoid being blown over by winds. Intercomparison testing tripods are visible in rear. The base bar attached to bottom of tower was used as a reference for height measurements.



Figure A-6. Sean O'Brien adjusts spacing of Li-Cor fast hygrometer with sonic anemometer to permit latent heat flux measurements.

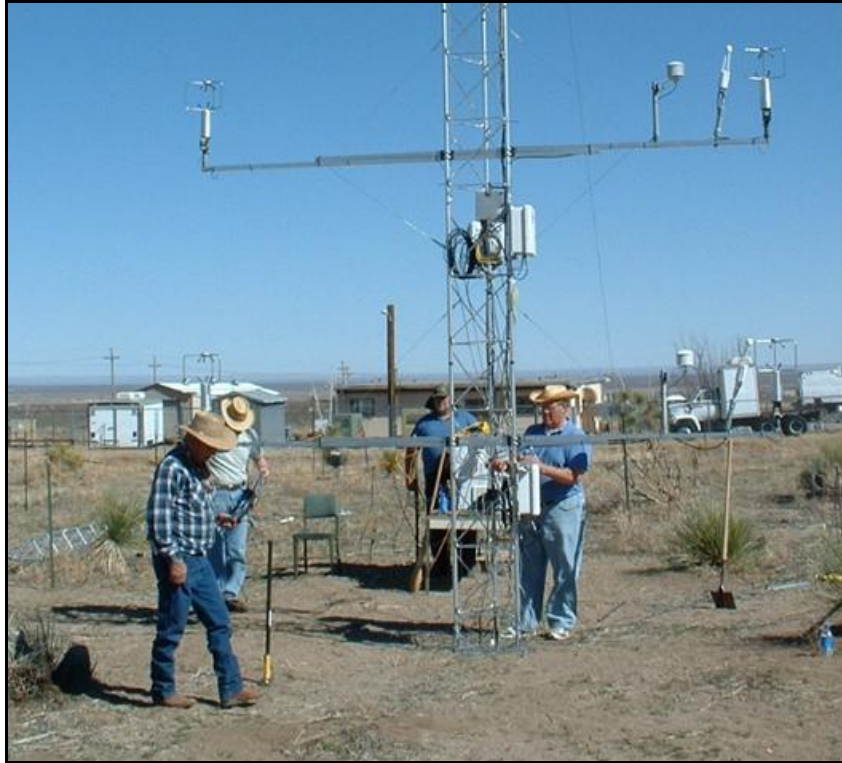


Figure A-7. Jimmy Yarbrough in foreground adjusting turnbuckle while performing final adjustments on flux profile tower for leveling.



Figure A-8. David Quintis stands between towers and Robert Brice wires instruments inside data acquisition box.

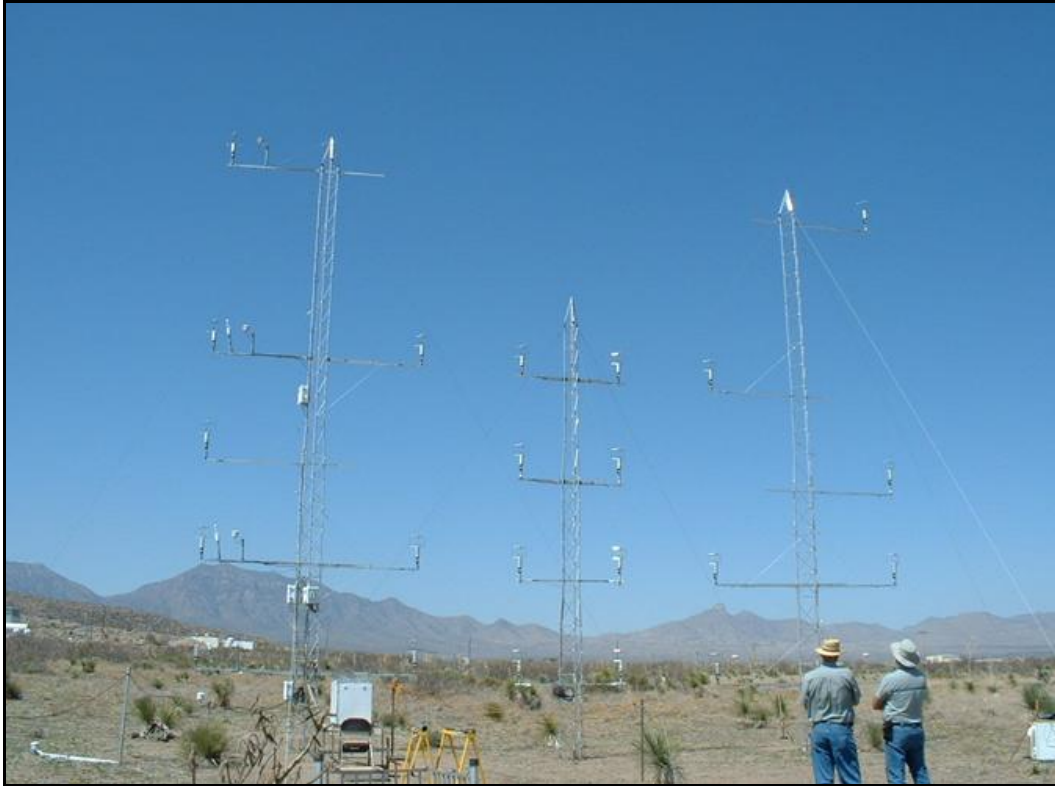


Figure A-9. Robert Brice and Edward Creegan inspect completed array looking west toward Baylor Pass (far left), Baylor Peak (just under [0, 4] flux profile sensors), San Augustin pass (behind central mast), and San Augustin Peak (just under [10, 04] sonic anemometer).

Intentionally Left Blank.

List of Symbols, Abbreviations, and Acronyms

1D	one-dimensional
2D	two-dimensional
3D	three-dimensional
3DTS	Three-Dimensional Turbulence Structure
AGL	above ground level
ARL	U.S. Army Research Laboratory
ASCII	American Standard Code for Information Interchange
BLT	Boundary Layer Turbulence
CO ₂	carbon dioxide
FFT	Fast Fourier Transform
FWHM	full-width half-width
HATS	Horizontal Array Turbulence Study
HELSTF	High Energy Laser System Test Facility
JD	Julian date
JU2003	Joint Urban 2003
K/m	degrees Kelvin per meter
LES	Large Eddy Simulation
met	meteorological
NCAR	National Center for Atmospheric Research
RTG-40	Research Technology Group 40
SBL	Stable Boundary Layer
SFS	subfilter-scale
TKE	Turbulent Kinetic Energy
WSMR	White Sands Missile Range

<u>No. of Copies</u>	<u>Organization</u>
1 PDF	ADMNSTR DEFNS TECHL INFO CTR DTIC OCP 8725 JOHN J KINGMAN RD STE 0944 FT BELVOIR VA 22060-6218
3 HCs	US ARMY RSRCH LAB ATTN RDRL CIM P TECHL PUB ATTN RDRL CIM L TECHL LIB ATTN IMNE ALC HRR MAIL & RECORDS MGMT 2800 POWDER MILL ROAD ADELPHI MD 20783-1197
1 CD	US ARMY RSRCH LAB ATTN RDRL CIM G TECHL LIB T LANDFRIED APG MD 21005-5066
1 CD	US ARMY RSRCH LAB ATTN RDRL ROE N W BACH PO BOX 12211 RESEARCH TRIANGLE PARK NC 27009
2 CDs	US ARMY RSRCH LAB ATTN RDRL CIE D S O'BRIEN WSMR NM 88002-5501
1 CD	US ARMY RSRCH LAB ATTN RDRL CIE M R SHIRKEY WSMR NM 88002-5501
1 CD	US ARMY RSRCH LAB ATTN RDRL CIE D D W HOOK WSMR NM 88002-5501
1 CD	ARMY MATERIEL SYSTEMS ANALYSIS ACTIVITY ATTN AMXSYS SC J MAZZ 392 HOPKINS ROAD APG MD 21005-5071

<u>No. of Copies</u>	<u>Organization</u>
1 CD	US ARMY NIGHT VISION & ELECTRONIC SENSORS DIRECTORATE MEASUREMENT AND MODELING SERVICES BRANCH ATTN AMSRD CER NV MS MMS J HIXSON 0221 BURBECK ROAD FT BELVOIR VA 22060-5806
1 CD	ARMY MODELING & SIMULATION OFFICE DA G37 DAMO SBM 400 ARMY PENTAGON WASHINGTON DC 20310-0450
2 CDs	US ARMY RSRCH LAB ATTN RDRL CIE D D TOFSTED WSMR NM 88002-5501
1 CD	DIRECTOR USA TRADOC ANALYSIS CENTER ATTN ATRC W P BLECHINGER WSMR NM 88002-5502
1 CD	DIRECTOR USA TRADOC ANALYSIS CENTER ATTN ATRC WA L SOUTHARD WSMR NM 88002-5502
1 CD	ERDC/CRREL ATTN G KOENIG 72 LYME RD HANOVER NH 03755
1 CD	ARMY CORPS OF ENGINEERS TOPOGRAPHIC ENGINEERING CENTER DATA AND SIGNATURE ANALYSIS BRANCH FT BELVOIR VA 22060

<u>No. of Copies</u>	<u>Organization</u>	<u>No. of Copies</u>	<u>Organization</u>
1 CD	US MILITARY ACADEMY DEPT OF MATHEMATICAL SCIENCES THAYER HALL WEST POINT NY 10996-1786	1 CD	NAVAL POSTGRADUATE SCHOOL J D EAGLE OR/ER 1 UNIVERSITY CIRCLE MONTEREY CA 93943
2 CDs	UNITED STATES MILITARY ACADEMY COMBAT SIMULATION LAB P WEST WEST POINT NY 10996	1 CD	NAVAL POSTGRADUATE SCHOOL R K WOOD OR/WD 1 UNIVERSITY CIRCLE MONTEREY CA 93943
1 CD	USA PEO STRI FCS TRAINING IPT ENVIRONMENT D STEVENS 12350 RESEARCH PKWY ORLANDO FL 32826-3276	1 CD	NAVAL POSTGRADUATE SCHOOL G SCHACHER DEPT OF PHYSICS 1 UNIVERSITY CIRCLE MONTEREY CA 93943
1 CD	AFRL/IFOIL 525 BROOKS ROAD ROME NY 13441-4505	1 CD	NAVAL POSTGRADUATE SCHOOL W B MAIER II DEPT OF PHYSICS 1 UNIVERSITY CIRCLE MONTEREY CA 93943
1 CD	AIR WEATHER SERVICE TECH LIBRARY FL4414 3 SCOTT AFB IL 62225-5458	1 CD	RUTH H HOOKER RESEARCH LIBRARY 4555 OVERLOOK AVE SW WASHINGTON DC 20375
1 CD	HQ USAFA/DFLIB 2354 FAIRCHILD DRIVE SUITE 3A10 USAF ACADEMY CO 80840-6214	1 CD	JWARS ATTN C BURDICK 1555 WILSON BOULEVARD SUITE 619 ARLINGTON VA 22209
1 CD	TECH CONNECT AFRL/XPTC BLDG 16 RM 107 2275 D STREET WPAFB OH 45433-7226	1 CD	NORTHROP GRUMMAN INFORMATION TECHNOLOGY M GOUVEIA 100 BRICKSTONE SQUARE ANDOVER MA 01810
1 CD	NAVAL RESEARCH LABORATORY A GOROCH MARINE METEOROLOGY DIVISION CODE 7543 7 GRACE HOPPER AVE MONTEREY CA 93943-5006	1 CD	NORTHROP GRUMMAN INFORMATION TECHNOLOGY H ISKENDERIAN 55 WALKERS BROOK DR READING MA 01867
1 CD	US NAVAL WAR COLLEGE WAR GAMING DEPARTMENT CODE 33 686 CUSHING ROAD NEWPORT RI 02841-1207		

<u>No. of Copies</u>	<u>Organization</u>	<u>No. of Copies</u>	<u>Organization</u>
1 CD	ANTEON CORP M ADAMS 46 GROWING RD HUDSON NH 03051	1 CD	R RASMUSSEN NATIONAL CENTER FOR ATMOSPHERIC RESEARCH P O BOX 3000 BOULDER CO 80307-3000
1 CD	SAIC ATTN MR DELGADO 731 LAKEPOINTE CENTRE DR O'FALLON IL 62269-3064	1 CD	E JACOBS THE UNIVERSITY OF MEMPHIS DEPARTMENT OF ELECTRICAL AND COMPUTER ENGINEERING 206 ENGINEERING SCIENCE BLDG. MEMPHIS TN 38152-3180
1 CD	TECHNICAL REPORTS BOULDER LABORATORIES LIBRARY MC 5 325 BROADWAY BOULDER CO 80305		
1 CD	NCAR LIBRARY SERIALS NATIONAL CENTER FOR ATMOSPHERIC RESEARCH PO BOX 3000 BOULDER CO 80307-3000	Total: 48 (1 PDF, 3 HCs, 43 CDs)	
1 CD	US ARMY NIGHT VISION & ELECTRONIC SENSORS DIRECTORATE SENSOR PERFORMANCE BRANCH ATTN AMSRD CER NV MS SP J REYNOLDS 10221 BURBECK ROAD FORT BELVOIR VA 22060-5806		
1 CD	US ARMY NIGHT VISION & ELECTRONIC SENSORS DIRECTORATE SENSOR PERFORMANCE BRANCH ATTN AMSRD CER NV MS SP R ESPINOLA 10221 BURBECK ROAD FT BELVOIR VA 22060-5806		
1 CD	US ARMY NIGHT VISION & ELECTRONIC SENSORS DIRECTORATE SENSOR PERFORMANCE BRANCH ATTN AMSRD CER NV MS SP M FRIEDMAN 10221 BURBECK ROAD FT BELVOIR VA 22060-5806		